IPP-Report

MAX-PLANCK-INSTITUT
FÜR PLASMAPHYSIK

Paul Huslage

Coherence of Turbulent Structures with Varying Drive in Stellarator Edge Plasmas

IPP 2023-10
November 2023

Coherence of Turbulent Structures with Varying Drive in Stellarator Edge Plasmas

Paul Huslage

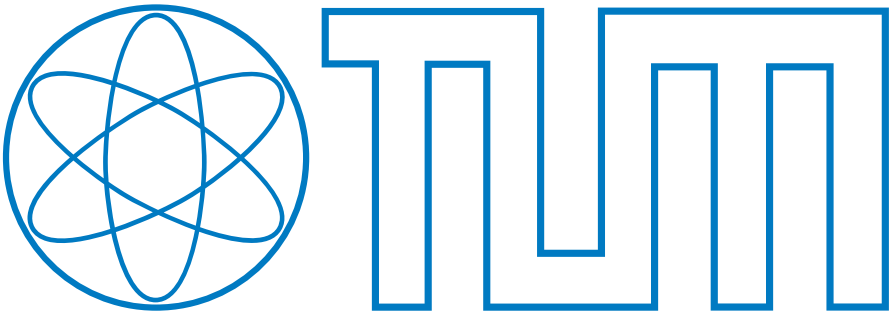

A thesis presented for the degree of
Master of Science (M.Sc)

under the supervision of Dr. Gregor Birkenmeier,
Technische Universität München,
on April 25th 2022.

To conclude (...) heating to thermonuclear temperatures should be possible (...), provided that the plasma is sufficiently quiescent.

Lyman Spitzer, The Stellarator Concept, 1958

However, the gas is definitely not quiescent.

Lyman Spitzer, The Stellarator Concept, 1958

Abstract

Nuclear fusion is a promising alternative for primary energy production. One approach to achieve fusion relevant conditions on earth is the magnetic confinement of high-temperature plasmas. Magnetic confinement fusion experiments suffer from losses through plasma turbulence. Filaments or blobs are a form of turbulent transport in the scrape-off layer (SOL) of toroidal fusion experiments.
This thesis investigates the parallel coherence of filaments by means of numerical simulations using the `hermes-2` model within the `BOUT++` framework. Under varying conditions a filament either stays a homogeneous structure parallel to the magnetic field or is ripped apart. Realistic field lines in the SOL of magnetic fusion devices, especially in stellarator configurations possess a highly varying curvature along the magnetic field line. A varying curvature drives inhomogeneous polarization along the field line. Hence, a parallel $\mathbf{E}\times\mathbf{B}$ velocity gradient arises which can tear the filament apart. The parallel potential gradient resulting from varying polarization drives the parallel current. If the latter flattens the parallel potential gradient fast enough the blob stays coherent. The main parameters controlling the propagation time of the parallel current are the collisionality and the electron plasma beta. These govern Ohmic and inductive resistance parallel to the magnetic field. A varying curvature reduces the propagation of a filament compared to a case with constant curvature.
Simulations of realistic curvature variations along field lines in a circular ASDEX Upgrade-like tokamak (AUG) and Wendelstein 7-X stellarator (W7-X) show the parallel displacement to correlate with the curvature. The varying W7-X curvature reduces the propagation of the filament to almost zero. The results are consistent with the previously found parametric dependencies for a sinusoidal curvature variation. This work supports experimental findings that filaments in W7-X are comparably slow due to the large major radius of the device. They do not perform ballistic motion and hence do not drive significant turbulence spreading in the SOL.

Zusammenfassung

Kernfusion ist eine vielversprechende Alternative als primäre Energiequelle. Ein Ansatz um fusionsrelevante Bedingungen auf der Erde zu erzeugen ist der magnetische Einschluss von Hochtemperaturplasmen. Magnetische Fusionsexperimente verlieren Teilchen und Wärme durch Plasmaturbulenz. Filamente oder Blobs sind eine Form des turbulenten Transports in der Abschälschicht von toroidalen magnetischen Einschlussexperimenten.
Diese Arbeit untersucht die parallele Kohärenz von Filamenten mit Hilfe numerischer Simulation des `hermes-2` Modells, welches Teil des `BOUT++` Frameworks ist. Unter verschiedenen Bedingungen bleib ein Filament entweder eine zusammenhängende Struktur parallel zum Magnetfeld oder wird auseinander gerissen. Realistische Feldlinien in der Abschälschicht von Fusionsexperimenten - insbesondere von Stellaratoren - zeigen eine stark entlang der Magnetfeldlinie variierende Krümmung. Eine variierende Krümmung treibt eine inhomogene Polarisation entlang der Feldlinie an. Dies führt zu einem parallelen Gradienten der $\mathbf{E} \times \mathbf{B}$ Drift, welcher das Filament auseinander reißen kann. Der parallele Potentialgradient, der aus der variierenden Polarisation entsteht, treibt einen parallelen Strom an. Wenn der parallele Strom den Potentialgradienten rechtzeitig auflöst, bleibt das Filament kohärent. Andernfalls wird es auseinander gerissen. Die wesentlichen Kontrollparameter für die Propagationszeit des parallelen Stroms sind die Kollisionalität und das Plasmabeta der Elektronen. Diese beiden Größen kontrollieren den Ohmschen und induktiven Widerstand parallel zur Feldlinie. Eine variable Krümmung reduziert die Geschwindigkeit eines Filaments verglichen mit einem Fall mit konstanter Krümmung. Simulationen mit realistischer Krümmungsvariation entlang von Feldlinien in einem kreisförmigen Tokamak mit ASDEX-Upgrade Parametern und im Wendelstein 7-X stellarator (W7-X) zeigen, dass die parallele Verschiebung mit der Krümmung korreliert. Die variable Krümmung der W7-X Feldlinie reduziert die Geschwindigkeit des Filaments auf quasi null. Diese Ergebnisse sind konsistent mit den zuvor entwickelten Parameterstudien mit sinusförmiger Krümmung. Diese Arbeit unterstützt experimentelle Erkenntnisse wonach Filamente in W-7X aufgrund des großen Radius der Machine langsam propagieren. Filamente zeigen keine ballistische Bewegung und treiben keine signifikante Ausbreitung der Turbulenz in die Abschälschicht an.

Dedication

This thesis would not have been possible without the support of great people who supported my in all the different stages of the project. First and foremost I have to thank Dr. Brendan Shanahan and Dr. Gregor Birkenmeier for their fantastic guidance and supervision along the whole way this work has gone.
The following document would be a lot worse without fantastic proofreaders. A special thanks goes to David Kulla, Jim-Felix Lobsien and Krzysztof Radacki. During the last three years I have been supported financially and ideationally by a scholarship from the Konrad-Adenauer Foundation (KAS), for which I am very grateful.

Contents

Chapter 1

Introduction

1.1 Nuclear Fusion

Energy is a foundation for human civilization and prosperity. The increase of energy available to humanity enables technological progress and a higher standard of living. Currently, energy is mostly provided by burning hydrocarbons into CO_2 [1].
Nuclear fusion presents a promising alternative as a primary energy source. It is anticipated to provide baseload energy from the fusion of deuterium ^{2}D and tritium ^{3}T nuclei into helium ^{4}He. For this fusion reaction to occur the positively charged nuclei must be fast enough to overcome the repulsive coulomb force. Once achieved, the strong nuclear force acts on a small length scale ($\sim 10^{-15}$m) and fuses the two isotopes, releasing a ^{4}He nucleus and a neutron. The difference in binding energy between products and reactants is distributed between the kinetic energies of the helium nucleus and the neutron according to momentum conservation

$$^3\mathrm{T} + {}^2\mathrm{D} \rightarrow {}^4\mathrm{He}\,(3.52\,\mathrm{MeV}) + {}^1\mathrm{n}\,(14.06\,\mathrm{MeV}). \tag{1.1}$$

In a nuclear fusion power plant the kinetic energy from the neutrons can be converted into heat which is used to drive steam turbines and create electricity. The energy of the α particle can be utilized to heat the remaining ^{2}D and ^{3}T fuel. Other reactions (e.g. $^3\mathrm{He} + {}^2\mathrm{D}$, $^1\mathrm{H} + {}^{11}\mathrm{B}$) are also possible but have much smaller cross sections with maxima at much higher temperatures and are therefore more difficult to achieve [2].
Deuterium is a stable isotope and can be drawn in abundance from seawater. Tritium decays with a halflife of 12.32 years [3]. It can be produced from lithium ^{6}Li or ^{7}Li in a blanket that will be part of commercial fusion power plants using the neutrons from the fusion reaction via

$$\begin{aligned} {}^6\mathrm{Li} + {}^1\mathrm{n} &\rightarrow {}^4\mathrm{He} + {}^3\mathrm{T} + 4.784\,\mathrm{MeV} \quad \text{or} \\ {}^7\mathrm{Li} + {}^1\mathrm{n} &\rightarrow {}^4\mathrm{He} + {}^3\mathrm{T} + {}^1\mathrm{n} - 2.467\,\mathrm{MeV}. \end{aligned} \tag{1.2}$$

Not all neutrons from the fusion reaction engage in tritium breeding. A self sufficient power plant demands the use of a neutron multiplier such as beryllium

$$^9\mathrm{Be} + {}^1\mathrm{n} \rightarrow 2\,{}^4\mathrm{He} + 2\,{}^1\mathrm{n} - 3.238\,\mathrm{MeV}\,[2]. \tag{1.3}$$

All isotopes needed for a fusion reaction (^{2}D and $^{6/7}$Li) are available copiously on earth to provide fusion energy for a practically infinite amount of time.
As a figure of merit, powering all of Germany's annual 559 TWh electricity demand

[4] exclusively by fusion would require about 10 tons of ^{2}D and 15 tons of ^{3}T, assuming a 30% conversion rate from neutron kinetic energy to electricity. The total energy demand is divided by the efficiency and the energy per reaction to get the number of fusion reactions necessary. Multiplying with the deuterium and tritium mass m_D and m_T gives the required amount of fuel

$$\frac{559 \cdot 10^{12}\,\mathrm{Wh}}{0.3 \cdot 14.06 \cdot 10^{6}\,\mathrm{eV}} \cdot \begin{pmatrix} m_D \\ m_T \end{pmatrix} \approx 3 \cdot 10^{30} \begin{pmatrix} m_D \\ m_T \end{pmatrix} \approx \begin{pmatrix} 10 \\ 15 \end{pmatrix} \cdot 10^{3}\,\mathrm{kg}. \tag{1.4}$$

Fuel in a fusion reactor needs to be constantly resupplied. Incidents halt the nuclear reaction and cannot lead to meltdowns or thermal runaways. Fusion could play a crucial role in the transition of the energy supply as a carbon-free, safe, base load capable source with high fuel energy density.

1.2 Plasma Confinement

The temperature T required for fusion to occur (about 10 keV) is orders of magnitude above the binding energy of electrons in the potential of atomic nuclei (about 10 eV).[1] Hence, atoms are fully ionized at these temperatures. Electrons and ions are not bound to each other and form a plasma, which is the most common state of matter in the universe.
Despite being composed of charged particles a fusion plasma is quasineutral on a macroscopic level. Local charge imbalances are shielded on the Debye length scale $\lambda_D = \sqrt{\epsilon_0 T/e^2 n}$. Here, n is the plasma density, ϵ_0 and e refer to the vacuum permittivity and the elementary charge. A plasma is assumed to be much larger than λ_D and the number of particles in a Debye cube of volume λ_D^3 to be much larger than 1. This ensures quasineutrality. The plasma exhibits collective effects as reaction to long-range electric and magnetic fields.
In the hydrogen plasmas investigated in this thesis ions are much heavier than electrons. Electrons with mass m_e perform oscillations against quasi-stationary ions with the plasma frequency $\omega_p = \sqrt{e^2 n/\epsilon_0 m_e}$. A thorough discussion of plasma dynamics is given in chapter 2.
To reach thermonuclear temperatures a plasma must be heated. For a power plant to produce a net energy output the power gained from the fusion reaction must be larger than the required heating power. This demands not only a sufficient temperature but an ample particle density and energy confinement time τ_E. The product of these three quantities needs to be above a certain threshold for a fusion reactor to deliver an energy surplus. A plasma is considered ignited if the heating is entirely provided by the α particles from the fusion reaction. This is formulated in the Lawson criterium [5]

$$nT\tau_E > 3 \cdot 10^{21}\,\mathrm{keV\,s\,m^{-3}}. \tag{1.5}$$

At a fixed temperature of ≈ 10 keV two main pathways exist to fulfill the above condition. Inertial confinement fusion aims at a high density and a comparably low confinement time. Pellets of fuel undergo a fast compression and fuse. The compressional force is provided by laser beams or via mechanical compression [6][7].

[1] In plasma physics the temperature T is usually given in the equivalent energy in eV.

Magnetic confinement fusion utilizes a magnetic field to confine the plasma. This approach leads to low densities but high energy confinement times. Magnetic confinement devices are the primary focus of this work.
In a magnetic field electrons and ions gyrate around the magnetic field lines which provides confinement perpendicular to the field. To avoid end losses the field lines are closed into a torus. The resulting magnetic field is not homogeneous leading to drifts and charge separations causing a loss of confinement. A poloidal magnetic field is required to short-circuit those charge imbalances and to provide sufficient plasma confinement. The combined helical magnetic field lines trace out surfaces on the poloidal cross section of the torus. These surfaces are called flux surfaces, as the toroidal magnetic flux enclosed by them is constant. For a plasma equilibrium in a toroidal confinement device the flux surfaces coincide with surfaces of constant pressure if the resistivity of the plasma is neglected.
There are two main types of magnetic fusion experiments differing mainly in their way of obtaining the poloidal field. Tokamaks have planar coils to create the toroidal field. They drive a toroidal current inside the plasma via a central solenoid to produce the additional poloidal field components. This introduces an additional source of free energy to the system which gives rise to disruptions and various other instabilities. A constantly induced current requires an ever increasing voltage in the solenoid which limits the operation time of conventional tokamaks.
There are developments for a stationary current drive by means of momentum transfer from tangentially injected fast particles [8]. A current can also be driven by coupling electromagnetic waves into the plasma, i.e. on the electron cyclotron resonance frequency or the lower hybrid resonance frequency (a longitudinal wave of electrons and ions). These methods are called Electron cyclotron/lower hybrid current drive (ECCD or LHCD), respectively. This approach is estimated to consume a significant portion of the output power of a commercial tokamak but could provide steady state confinement in a tokamak [9].
The stellarator is the other main toroidal magnetic field configuration. It creates its poloidal field by breaking the axisymmetry of the magnetic field. This results in non-planar coils creating both toroidal and poloidal field components. These coils pose a significant engineering challenge. Early stellarators showed very poor performance compared to tokamaks due to strong so-called neoclassical transport arising from the non-axisymmetric magnetic field. The experiments Wendelstein 7-AS, HSX and Wendelstein 7-X showed that numerical optimization of the coils reduces neoclassical transport and enables plasma confinement similar to tokamaks [10][11][12][13]. A stellarator is intrinsically steady-state capable and disruption free.
Current tokamaks and optimized stellarators are mostly limited in their performance by turbulent transport. Steep pressure gradients at the boundary of the confined plasma region drive turbulent instabilities which lead to outward heat and particle transport. This reduces the confinement time and creates high heat loads on the plasma facing components. Stellarators possess significantly more degrees of freedom in magnetic field design compared to tokamaks. This facilitates computational optimization which aims to decrease turbulent transport in stellarators and to possibly exceed the performance of similarly sized tokamaks [14][15][16].
Beyond the last closed flux surface in a tokamak or stellarator, particles and heat are primarily funneled along open field lines onto divertor plates which can sustain the high heat flux where they are extracted from the device. This region is the

scrape-off layer (SOL) where perpendicular transport is dominated by filaments or blobs which are the main focus of this thesis [17][18][19].

1.3 Scope of this Thesis

The main topic of this thesis is the coherence of turbulent structures or blobs in the SOL of stellarator plasmas. Heat and particles are transported radially outwards by these structures. A common simplification is to assume blobs to be homogeneously elongated along a magnetic field line. This thesis investigates the limits of this assumption. The propagation of filaments is affected by the inhomogeneous nature of the stellarator's magnetic field, particularly its curvature. The varying curvature leads to an inhomogeneous drive for the filament propagation parallel to the magnetic field. Parallel ohmic and inductive resistance limit the parallel current in resolving this difference. These different effects decide whether a filament stays coherent along a magnetic field line and are the focus of this thesis.
This chapter offered an overview on nuclear fusion, its relevance, mechanism and technical execution. Chapter 2 features the differential equations used in this work to model plasmas at the edge of fusion devices using the hot-ion `hermes-2` model. Chapter 3 presents the primary characteristics behind turbulence in neutral fluids and plasmas. It describes the main regimes of plasma dynamics in a toroidal magnetic fusion experiment and focuses on the scrape-off layer and the propagation of filaments. An overview on filament research in stellarators is presented. Chapter 4 introduces the `BOUT++` framework which is used to simulate the `hermes-2` model equations. It presents differential operators and initial conditions for the numerical simulations performed in this thesis and validates them with the different scalings of the filament velocity with their size. The main effects determining the coherence of a filament along a field line are investigated in Chapter 5. This is applied to realistic geometries in the following chapter 6. Numerical simulations are performed for a circular tokamak field line and a field line in the W7-X SOL. Chapter 7 summarizes the findings and discusses them in the context of previous research.

Chapter 2

Plasma Dynamics

This chapter establishes the mathematical basis for modeling plasmas in the scrape-off layer. First, the motion of single, charged particles in a magnetic field is introduced. Section 2.2 discusses the collective description of plasmas and simplifies the Boltzmann equation to the Braginskii fluid equations. The last section deals with the assumptions specific to the `hermes-2` model used in this thesis and gives its evolution equations which are used in the following numerical simulations. The influence of classical diffusion is briefly visited.

2.1 Single Particle Motion

The motion of a charged particle with charge q, mass m and velocity $\mathbf{v}$ in a magnetic field $\mathbf{B}$ is governed by the Lorentz force

$$m\dot{\mathbf{v}} = q\left(\mathbf{E} + \mathbf{v} \times \mathbf{B}\right) + \mathbf{F}. \tag{2.1}$$

Particles perform a gyration around the magnetic field lines in the absence of electric fields $\mathbf{E}$, other forces $\mathbf{F}$ and in a homogeneous magnetic field. Perpendicular to the field they circle around the field line with the cyclotron frequency $\omega_c = qB/m$ and the Larmor radius $\rho = \sqrt{2Tm}/|q|B$. Parallel to the magnetic field particles move freely with their initial parallel velocity component $v_\parallel$[1]. For many applications, only the guiding center motion of the particle's trajectory after averaging over one gyroperiod ($\langle\mathbf{v}\rangle = \frac{\omega_c}{2\pi}\int_0^{2\pi/\omega_c} \mathbf{v}\, dt$) is considered. An electric field, other forces or inhomogeneities in the magnetic field cause drifts of the guiding center. Drift components $\langle\mathbf{v}_\perp\rangle$ perpendicular to the magnetic field can lead to charge separation inside the plasma causing a loss of confinement.
Averaging over ensembles of many particles leads to the fluid picture of plasmas which serves as a collective description of plasma dynamics. This will be discussed in the next section and is used in the remainder of the thesis. Single particle drifts must not simply be transferred to a collective picture without proper averaging. Drifts in fluid models have a different mathematical appearance while displaying similar physical mechanisms compared to drifts in the single particle picture [20].

[1] $\mathbf{v} = \mathbf{v}_\parallel + \mathbf{v}_\perp; \quad \mathbf{v}_\parallel = (\mathbf{v}\cdot\mathbf{B})\,\mathbf{B}/B^2; \quad v_\parallel = \mathbf{b}\cdot\mathbf{v}$

2.2 Fluid Models

A plasma not subject to quantum or relativistic effects can be described by a phase-space distribution function $f_s(\mathbf{z}, t)$ for each particle species s displaying the particle density at a given point $\mathbf{z} = (\mathbf{x}, \mathbf{v})$ in phase space across time t. Its evolution is described by a continuity equation

$$\partial_t f_s + \nabla_{\mathbf{z}}(\dot{\mathbf{z}} f_s) = 0. \tag{2.2}$$

with $\dot{\mathbf{z}} = (\mathbf{v}, \dot{\mathbf{v}})$ and the gradient with respect to position and velocity $\nabla_{\mathbf{z}} = (\nabla_{\mathbf{x}}, \nabla_{\mathbf{v}})$. This can be expanded by inserting $\dot{\mathbf{v}} = \mathbf{F}/m_s$ and splitting the force term into the Lorentz force and short-range forces from collisions $C_{s,s'}$ between different species s and s'. This leads to the Boltzmann equation[2]

$$\partial_t f_s + \mathbf{v}_s \cdot \nabla_{\mathbf{x}} f_s + \frac{q_s}{m_s} (\mathbf{E} + \mathbf{v} \times \mathbf{B}) \cdot \nabla_{\mathbf{v}} f_s = \sum_{s'} C_{s,s'}. \tag{2.3}$$

Solving equation 2.3 provides a full kinetic description of the plasma dynamics. Treating a problem with seven degrees of freedom at a sufficient resolution is a computationally expensive task. There are different paths to simplify this equation. Fusion plasmas are usually strongly magnetized [20]. The Larmor radius ρ is much smaller than any macroscopic length scale. Averaging the Boltzmann equation over the gyromotion reduces the dimensionality of the problem by one. Gyrokinetic codes such as `GENE` exert this method to describe plasma turbulence in the core of magnetic fusion devices [14][21][22]. As this thesis is concerned with turbulence on the edge of fusion plasmas which is characterized by higher collisionality it utilizes a different approach. Higher collisionality facilitates formation of local thermal equilibria for a single particle species implying a Maxwell-Boltzmann distribution of the velocity. Taking the moments of the Boltzmann equation with respect to the velocity leads to a system of equations describing the evolution of averaged quantities such as the particle density n_s and the fluid velocity $\mathbf{u}_s$

$$n_s = \int f_s \, \mathrm{d}^3 v, \quad \mathbf{u}_s = \frac{1}{n_s} \int \mathbf{v} f_s \, \mathrm{d}^3 v. \tag{2.4}$$

The n-th moment of equation 2.3 is taken by multiplication with the n-th power of the velocity and integration over velocity space $\int \mathbf{v}^n (\cdots) \, \mathrm{d}^3 v$. This ansatz results in the Braginskii equations which form the basis of several plasma turbulence models like `GRILLIX` and `hermes` [23][24][25].
The zeroth moment of the Boltzmann equation results in the continuity equation

$$\partial_t n_s + \nabla \cdot (n_s \mathbf{u}_s) = 0. \tag{2.5}$$

As the velocity dependence is averaged out, the gradient ∇ is only taken with respect to space. The first moment gives the equation of motion

$$n_s m_s (\partial_t + \mathbf{u}_s \cdot \nabla) \mathbf{u}_s = -\nabla p_s - \nabla \cdot \mathbf{\Pi}_s + q_s n_s (\mathbf{E} + \mathbf{u} \times \mathbf{B}) + \sum_{s' \neq s} \mathbf{F}_{s',s}. \tag{2.6}$$

Changes in momentum can be driven by a pressure gradient ∇p_s, the friction force between different species s and s' or a finite divergence of the viscous stress tensor

[2] using $\nabla_{\mathbf{x}} \cdot \mathbf{v} = 0$ and $\nabla_{\mathbf{v}} \cdot (\mathbf{E} + \mathbf{v} \times \mathbf{B}) = 0$

$\mathbf{\Pi}_s = m_s n_s \mathbf{v} \otimes \mathbf{v}$ using the dyadic product $(\mathbf{v} \otimes \mathbf{v})_{i,j} = v_i v_j$. The tensor components $m_s n_s v_i v_j$ represent the flux of the i-th momentum component in the j-th direction. It can be split into contributions from parallel, perpendicular and gyromotion

$$\mathbf{\Pi}_s = \mathbf{\Pi}_{\parallel,s} + \mathbf{\Pi}_{\perp,s} + \mathbf{\Pi}_{g,s}. \tag{2.7}$$

The perpendicular and parallel contributions $\mathbf{\Pi}_{\perp,s}$ and $\mathbf{\Pi}_{\parallel,s}$ are small compared to the gyroviscous part $\mathbf{\Pi}_{g,s}$ and are ignored in the following `hermes-2` model equations. $F_{s,s'}$ denotes the friction force between different species s and s'. The evolution equation for the temperature T_s is obtained from the second moment

$$\frac{3}{2} n_s \left(\partial_t + \mathbf{u}_s \cdot \nabla\right) T_s = -\nabla \cdot \mathbf{q}_s - n_s T_s \nabla \cdot \mathbf{u}_s - \mathbf{\Pi}_s \otimes \nabla \mathbf{u}_s + \sum_{s' \neq s} W_{s',s}. \tag{2.8}$$

The temperature in the co-moving frame of the fluid changes in time by a finite divergence of the heat flux $\mathbf{q}_s$, compression of the fluid flow, internal viscosity and energy exchange between different particle species $W_{s,s'}$.
The turbulent closure problem manifests in the above system of equations. By construction, the n-th moment always encompasses a quantity whose evolution can only be found by constructing the (n+1)-th moment. The continuity equation involves the fluid velocity which is evolved in the first moment which depends on the pressure ($p_s = n_s T_s$). The temperature evolution depends on the heat flux $\mathbf{q}_s$ which is a third-order quantity. At some point the series has to be truncated and an evolution equation for the next order quantity needs to be found from physical reasoning to close the system.
Applying the cross product with $\mathbf{B}$ to equation 2.6 and neglecting terms for internal viscosity and collisions with other particle species results in an expression for the perpendicular drifts $\mathbf{u}_\perp$ in fluid models

$$\mathbf{u}_\perp = \frac{\mathbf{E} \times \mathbf{B}}{B^2} - \frac{\nabla p_s \times \mathbf{B}}{q_s n_s B^2} - \frac{m_s}{q_s B} \left(\partial_t \mathbf{u}_s + \left(\mathbf{u}_s \cdot \nabla\right) \mathbf{u_s}\right) \times \mathbf{B}. \tag{2.9}$$

This expression uses $(\mathbf{u} \times \mathbf{B}) \times \mathbf{B} = -\mathbf{u}_\perp B^2$. The first term of equation 2.9 is the $\mathbf{E} \times \mathbf{B}$ drift $\mathbf{u_E}$. It is charge independent and creates no current except for high frequencies which are not relevant for this thesis. The second term is the diamagnetic drift $\mathbf{u}_{dia,s}$. Pressure gradients create a charge dependent drift which can result in an electric field. The third term is the polarization drift $\mathbf{u}_{pol,s}$. The polarization drift is the smallest of the drifts due to its prefactor m_s/q_s. Perturbation theory can be applied to express it independent from the velocity. This thesis utilizes a second order expression for the polarization drift [20]

$$\mathbf{u}_{pol,s} = \frac{m_s \dot{\mathbf{E}}_\perp}{q_s B} - \frac{m_s \nabla_\perp \dot{p}_s}{n_s q_s^2 B^2}. \tag{2.10}$$

It is neglected in the continuity equation. The current it produces plays an important role in ensuring quasineutrality and needs to be included in $\nabla \cdot \mathbf{j} = 0$ resulting in equation 2.22. As $\mathbf{u}_{pol,e}$ is smaller than $\mathbf{u}_{pol,i}$ by a factor of m_e/m_i its contribution to the current balance is discarded.

2.3 hermes-2

The `hermes-2` model used in this thesis is based on the first three moments of the Boltzmann equation 2.3 given above. These equations have to be formulated for electron and ions. A number of simplifications and approximations has to be applied. The model is based on the equations introduced by Simakov and Catto [26]. Their ordering is discussed in the following to motivate the equations and the regime of plasma physics they are valid for. A rigorous derivation of the model equations is beyond the scope of this thesis.
The plasma is assumed to feature two separate length scales. The slowly varying scale L_s connected to the curvature and gradients of the equilibrium magnetic field and the quickly varying length scale L_f of the radial pressure gradients ($L_s \sim R_0 \sim a \gg L_f$). The major and minor radius of the toroidal plasma experiment are denoted by R_0 and a. The ratio between the length scales is therefore

$$\epsilon = \frac{L_f}{L_s} \ll 1. \tag{2.11}$$

The turbulent fluctuations are assumed to be strongly field aligned ($k_\parallel \ll k_\perp$) implying $k_\parallel \sim L_s^{-1}$ and $k_\perp \sim L_f^{-1}$ for the parallel and perpendicular wavenumbers. The ratio between thermal and magnetic pressure - the plasma beta

$$\beta = \frac{2\mu_0 p}{B^2} \ll 1 \tag{2.12}$$

is assumed to be small. Fluctuations of plasma quantities as density or pressure are assumed to be on the order of the equilibrium quantities. The fluctuations of the magnetic field are consequently smaller by a factor of β compared to the equilibrium magnetic field. Considering a magnetized, collisional plasma two small quantities are defined to be of similar size

$$\delta_s = \frac{\rho_s}{L_f} \approx \Delta_s = \frac{\lambda_s}{L_s} \ll 1. \tag{2.13}$$

$\lambda_s = v_{th,s}/\nu_s$ is the mean free path length of a species with the thermal velocity $v_{th,s} = \sqrt{2T_s/m_s}$ and the typical collision frequency ν_s. The Larmor radius is small compared to the fast scale of the gradient scale. The mean free path length is small compared to the scale of the device.
In order to include neoclassical expressions for the current, radial ion heat flux and parallel ion velocity, terms are kept that are valid only for $\delta_i \ll \Delta_i$. This contradicts the ordering but keeps important physical effects [26]. The frequencies are ordered as

$$|\omega_{c,s}| \gg \nu_s \gg \Omega \sim \delta_i^2 \omega_{c,i}. \tag{2.14}$$

with Ω being the frequency of the physics of interest. The flow velocity u_s is assumed to be small compared to the ion thermal velocity $v_{th,i}$. As in the presence of turbulence $v_{\parallel,i} \sim (\epsilon/\delta_i)\, v_{th,i}$ it is required that $\epsilon \ll \delta_i$. Equation 2.14 leads to $\epsilon \gg \delta_i \Delta_i$

$$\nu_i \gg \delta_i^2 \omega_{c,i} \Leftrightarrow \frac{v_{th,i}\rho_i}{c_i \lambda_i} \gg \delta_i^2 \Leftrightarrow \frac{v_{th,i}}{c_i}\frac{\delta_i L_f}{\Delta_i L_s} \gg \delta_i^2 \Rightarrow \epsilon \gg \delta_i \Delta_i, \tag{2.15}$$

assuming ion thermal velocity and sound speed to be of similar magnitude. Therefore,

$$\delta_i \gg \epsilon \gg \delta_i \Delta_i. \tag{2.16}$$

The `hermes-2` model is the plasma fluid model used in this work. It is an extension of the `hermes` model factoring in effects of a finite, evolving ion temperature T_i [24][27]. It uses the assumptions of a small β, magnetized, collisional plasma presented above to simplify the Bragisnkii equations from section 2.2. The resulting model equations evolve density n, electron pressure p_e, ion pressure p_i, parallel ion momentum $nv_{\parallel,i}$, vorticity ω as well as the electrostatic potential ϕ and the parallel component of the vector potential ψ. The model also includes terms for interaction with neutral particles which are dropped in the following as this thesis is not concerned with neutral physics.
In fluid and plasma turbulence it is useful to introduce the vorticity ω as the rotation of the velocity

$$\omega = \nabla \times \mathbf{u}. \tag{2.17}$$

It is also convenient to introduce the magnetic unit vector $\mathbf{b} = \mathbf{B}/B$. The gradient operator of a scalar function f can be split up into parallel and perpendicular components $\nabla f = \nabla_\perp f + \nabla_\parallel f$ with $\nabla_\parallel f = (\nabla f \cdot \mathbf{b})\,\mathbf{b}$ and $\nabla_\perp f = \nabla f - \nabla_\perp f$. In later equation the parallel derivative $\partial_\parallel f = \mathbf{b} \cdot \nabla f$ is needed. Wherever possible the diamagnetic drift is replaced by the magnetic drift

$$\mathbf{v}_{mag,s} = -\frac{T_e}{q_s}\left(\nabla \times \frac{\mathbf{b}}{B}\right) \tag{2.18}$$

which is numerically adventageous [24]. It replaces the diamagnetic drift e.g. in the density equation where the relevant term is identical

$$\nabla \cdot (n\mathbf{v}_{mag,e}) = -\frac{1}{e}\left(\nabla \times \frac{\mathbf{b}}{B}\right) \cdot \nabla p_e = \nabla \cdot (n\mathbf{v}_{dia,e})\,. \tag{2.19}$$

The density evolution reads

$$\partial_t n = -\nabla \cdot (n\mathbf{v}_\mathbf{E} + n\mathbf{v}_{mag,e}) - \nabla_\parallel \left(nv_{\parallel,e}\right). \tag{2.20}$$

The RHS terms correspond to the divergence of the particle fluxes from $\mathbf{E} \times \mathbf{B}$, diamagnetic drifts and parallel velocity. The polarization drift from equation 2.10 is discarded as it is smaller by a factor of $\omega_{c,s}$. However, the resulting ion polarization current is accounted for in the vorticity evolution 2.22.
The vorticity is simplified via the Bousinessq approximation which replaces the density with a constant value n_0 assuming density fluctuations to be much smaller than potential fluctuations so that $\nabla \cdot (n\partial_t \nabla_\perp \phi) \approx n_0 \partial_t \nabla_\perp^2 \phi$ [28]. The vorticity reads

$$\omega = \nabla \cdot \left(\frac{1}{B^2}\left(n_0 \nabla_\perp \phi + \nabla_\perp p_i\right)\right). \tag{2.21}$$

This approximation is found not to have much impact on the dynamics of turbulent plasma fluid simulations but improves computation time significantly [29]. The

vorticity equation

$$\begin{aligned}\partial_t\omega = &\nabla\cdot\left(\left(p_e+p_i\right)\nabla\times\frac{\mathbf{b}}{B}\right)+\nabla_\parallel j_\parallel \\ &-\nabla\cdot\left(\frac{1}{2B^2}\nabla_\perp\left(\mathbf{v_E}\cdot\nabla p_i\right)+\frac{\omega}{2}\mathbf{v_E}+\frac{n_0}{2B^2}\Delta_\perp\phi\left(\mathbf{v_E}+\mathbf{v}_{dia,i}\right)\right) \\ &+\nabla\cdot\left(\frac{\pi_{ci}}{2}\nabla\times\frac{\mathbf{b}}{B}-\frac{1}{3}\frac{\mathbf{b}\times\nabla\pi_{ci}}{B}\right).\end{aligned} \tag{2.22}$$

results from quasineutrality ($\nabla\cdot\mathbf{j}=0$). The first three terms represent the divergence of the diamagnetic, parallel and polarization current respectively. The additional contributions include cross-field and parallel viscosity.
The scalar gyroviscous stress tensor for ions is given by [27]

$$\begin{aligned}\pi_{ci} = &\frac{3m_i}{4p_iT_i}\left(0.20q_{\parallel,i}^2-0.085q_i^2\right) \\ &+0.96\frac{p_i}{\nu_i}\kappa\cdot\left(\mathbf{v_E}+\mathbf{v}_{di}+1.61\frac{\mathbf{b}\times\nabla T_i}{B}\right) \\ &-\frac{2}{\sqrt{B}}\partial_\parallel\left(\sqrt{B}v_{\parallel,i}\right)-\frac{1.42}{p_i\sqrt{B}}\partial_\parallel\left(\sqrt{B}q_{\parallel,i}\right) \\ &-\frac{0.49q_{\parallel,i}}{p_i}\left(2.27\partial_\parallel\ln T_i-\partial_\parallel\ln p_i\right).\end{aligned} \tag{2.23}$$

The numerical prefactors in the ion gyroviscous stress tensor are derived by Bragisnkii [30]. The closures of this system is given by the parallel and total ion heat fluxes[27]

$$q_{\parallel,i}=-\kappa_{\parallel,i}\partial_\parallel T_i,\quad q_i^2=\left(\kappa_{\parallel,i}^2-\left(\frac{5}{2}p_i\right)^2\right)\left(\partial_\parallel T_i\right)^2+\left(\frac{5}{2}p_i\nabla T_i\right)^2. \tag{2.24}$$

These expression are the Spitzer-Harm heat fluxes used in the popular transport code `SOLPS` [31].

$$\begin{aligned}\frac{3}{2}\partial_t p_e = &-\nabla\cdot\left(\frac{3}{2}p_e\mathbf{v_E}+\frac{5}{2}p_e\mathbf{v}_{mag,e}\right)-p_e\nabla\cdot\mathbf{v_E} \\ &-\nabla\cdot\left(\frac{3}{2}p_ev_{\parallel,e}\right)-p_e\nabla_\parallel v_{\parallel,e}+\nabla_\parallel\left(\kappa_{\parallel,e}\partial_\parallel T_e\right) \\ &+0.71\nabla_\parallel\left(T_ej_\parallel\right)-0.71j_\parallel\partial_\parallel T_e+\frac{\nu}{n}j_\parallel^2 \\ &+\nabla\cdot\left(\frac{\rho_e^2}{\tau_e}\left(\nabla_\perp p_e+\nabla_\perp p_i+\frac{11}{12}n\nabla_\perp T_e\right)\right)-W_i.\end{aligned} \tag{2.25}$$

The electron pressure evolution includes advection by perpendicular and parallel drifts as well as compression of $\mathbf{E}\times\mathbf{B}$ and parallel flows. There are terms for parallel heat conduction, thermal force and thermal currents. It features collisional cross-field transport on the scale of the Larmor radius and the electron collision time τ_e. The collisional energy exchange between electrons and ions is given by

$$W_i=\frac{3m_e}{m_i}\frac{n\left(T_e-T_i\right)}{\tau_e}.$$

The ion pressure evolution encompasses similar expressions for advection by and compression of drifts and parallel velocity. The following terms are energy exchange with diamagnetic flows, parallel viscous heating, parallel and perpendicular collisional heat conduction, collisional resistive drift, heating via perpendicular viscosity and collisional energy exchange with electrons:

$$\begin{aligned}\frac{3}{2}\partial_t p_i = &- \nabla\cdot\left(\frac{3}{2}p_i\mathbf{v_E} + \frac{5}{2}p_i\mathbf{v}_{mag,i}\right) - p_i\nabla\cdot\mathbf{v_E} \\ &- \nabla\cdot\left(\frac{3}{2}p_i\mathbf{b}v_{\parallel,i}\right) - p_i\nabla_\parallel v_{\parallel,i} - \frac{j_\parallel}{n_0}\partial_\parallel p_i \\ &+ \frac{p_i}{n_0}\nabla\cdot\left(\left(p_e+p_i\right)\nabla\times\frac{\mathbf{b}}{B}\right) + v_{\parallel,i}\frac{2}{3}B^{\frac{3}{2}}\partial_\parallel\left(\frac{\pi_{ci}}{B^{3/2}}\right) \\ &+ \nabla_\parallel\left(\kappa_{\parallel,i}\partial_\parallel T_i\right) + \nabla\cdot\left(\kappa_{\perp,i}\nabla_\perp T_i\right) \\ &+ \frac{5}{2}\nabla\cdot\left(\frac{T_i\rho_e^2}{T_e\tau_e}\left(\nabla_\perp p_e + \nabla_\perp p_i - \frac{3}{2}n\nabla_\perp T_e\right)\right) \\ &- \frac{3T_i}{10\tau_i B^2}\nabla_\perp\omega\cdot\nabla\left(\phi + \frac{p_i}{n_0}\right) \\ &- \left(\frac{\pi_{ci}}{2}\nabla\times\frac{\mathbf{b}}{B} - \frac{1}{3}\frac{\mathbf{b}\times\nabla\pi_{ci}}{B}\right)\cdot\nabla\left(\phi + \frac{p_i}{n_0}\right) + W_i.\end{aligned} \tag{2.26}$$

The parallel and perpendicular ion heat conduction coefficients are given by

$$\kappa_{\parallel,i} = 3.9\frac{p_i\tau_i}{m_i} \quad \kappa_{\perp,i} = 2\frac{n\rho_i^2}{\tau_i}. \tag{2.27}$$

Here, τ_i is the ion collision time. The parallel ion momentum equation

$$\begin{aligned}\partial_t\left(nv_{\parallel,i}\right) = &- \nabla\cdot\left(nv_{\parallel,i}\left(\mathbf{v_E} + \mathbf{b}v_{\parallel,i} + \mathbf{v}_{mag,i}\right)\right) \\ &- \partial_\parallel p_e - \partial_\parallel p_i - \frac{2}{3}B^{\frac{3}{2}}\partial_\parallel\left(\frac{\pi_{ci}}{B^{3/2}}\right) \\ &+ \nabla\cdot\left(v_{\parallel,i}\frac{\rho_e^2}{\tau_e T_e}\left(\left(T_e+T_i\right)\nabla_\perp n + n\left(\nabla_\perp T_i - \frac{1}{2}\nabla_\perp T_e\right)\right)\right).\end{aligned} \tag{2.28}$$

has terms for advection by the $\mathbf{E}\times\mathbf{B}$ drift, ion magnetic drift and parallel flow. It comprises of parallel electron and ion pressure gradients, parallel ion viscosity as well as collisional transport. Parallel currents $j_\parallel$ are evolved according to Ohm's law

$$\begin{aligned}\partial_t\left(\frac{m_e}{m_i}\left(v_{\parallel,e} - v_{\parallel,i}\right) + \frac{1}{2}\beta_e\psi\right) = &\partial_\parallel\phi - \frac{1}{n}\partial_\parallel p_e - 0.71\partial_\parallel T_e + \frac{\nu j_\parallel}{n} \\ &+ \frac{m_e}{m_i}\left(\mathbf{v_E} + \mathbf{b}v_{\parallel,i}\right)\cdot\nabla\left(v_{\parallel,i} - v_{\parallel,e}\right).\end{aligned} \tag{2.29}$$

It encompasses an electromagnetic induction term which is controlled by the electron plasma beta $\beta_e = 2\mu_0 nT_e/B^2$. Currents can be driven by parallel gradients in potential, pressure and temperature or a difference in electron and ion parallel velocity. The `hermes-2` model conserves the particle number $N = \int \mathrm{d}V\, n$ and an

energy E

$$E = \int \mathrm{d}V \, \frac{m_i n_0}{2} \left| \frac{\nabla_\perp \phi}{B} + \frac{\nabla_\perp p_i}{e n_0 B} \right|^2 + \frac{1}{2} m_i n v_{\parallel,i}^2 + \frac{3}{2} \left(p_i + p_e \right) + \frac{1}{4} \beta_e \left| \nabla \psi \right|^2 + \frac{m_i}{2 m_e} \frac{j_\parallel}{n}. \tag{2.30}$$

The first three terms are ion kinetic energy from $\mathbf{E} \times \mathbf{B}$, diamagnetic and parallel flows. Electron kinetic energy can be neglected as its smaller by a factor m_e/m_i. Additional contributions come from ion and electron thermal energy as well as the electromagnetic energy.
`hermes-2` contains self-consistent expressions for classical diffusion in the equations for density, vorticity, electron and ion pressure as well as parallel momentum. This avoids the introduction of unphysical, numerical diffusion coefficients [32]. These terms are motivated by a classical random walk ansatz for the particle motion perpendicular to the magnetic field. The typical increment is the Larmor radius. For example, the diffusion term for the electron pressure reads

$$\partial_t p_e = ... + \nabla \cdot \left(\frac{\rho_e^2}{\tau_e} \left(\nabla_\perp p_e + \nabla_\perp p_i + \frac{11}{12} n \nabla_\perp T_e \right) \right). \tag{2.31}$$

Contributions from classical diffusion are very small. Figure 2.1 shows the density

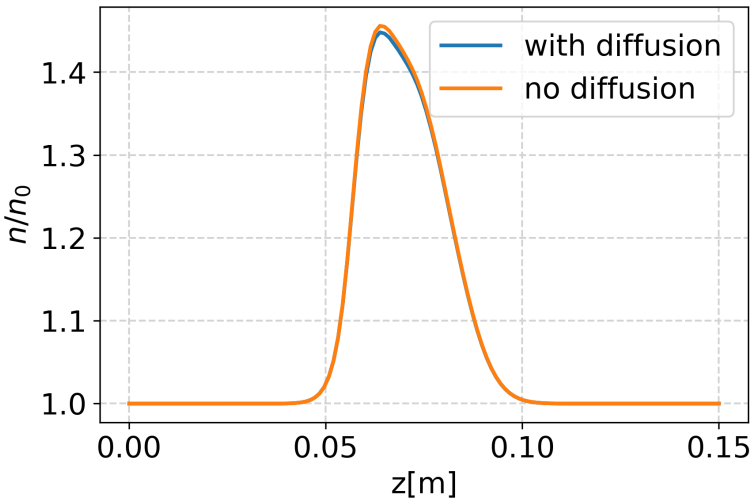

Figure 2.1: The influence of classical diffusion on a filament simulation after $1000/\Omega_{c,i}$. Contributions from diffusion terms lead to a faster flattening of a pressure perturbation. This effect is very small compared to turbulent advection.

profile of a filament simulation presented in the later chapters for two cases. The classical diffusion coefficients are set to zero for one of the two simulations. If classical diffusion is turned on the density peak is slightly lower as it diffuses into the area of lower density. This effect is small compared to the convective terms in the equations after a relevant timescale $(1000/\omega_{c,i})$.
This chapter discussed the foundation to model plasmas in low β, collisional, magnetized plasma as they are found in the edge and scrape-off layer of fusion plasmas. Turbulence and filaments are discussed in the next chapter establishing the main research topic of this thesis.

Chapter 3

Plasma Turbulence and Coherent Structures

This chapter introduces filaments - a source of turbulent losses in toroidal magnetic fusion devices. Filaments are the main topic of this work. A visit to the basic concepts of turbulence in neutral fluids in section 3.1 is followed by an introduction to the main regimes of turbulence in toroidal magnetic fusion experiments in section 3.2 from the core to the plasma edge and scrape-off layer where filaments are born and propagate. Section 3.4 discusses the basic mechanisms and scalings of filament motion. Simplified scaling laws for the velocity are derived in 3.5. Sections 3.6 and 3.7 discuss the effects of a varying curvature and the parallel current evolution on filament dynamics. Section 3.8 gives an overview of the research on filaments in stellarators.

3.1 Turbulence in Neutral Fluids

Turbulence is a phenomenon of fluid motion. Fluctuations over a wide range of length scales produce a chaotic, seemingly arbitrary behavior. Turbulence happens on all scales in nature. It appears in the gas clouds of galaxies, the convection zone of stars, the storms in the atmosphere of Jupiter or the mixing of milk and coffee in a cup.
A complete quantitative understanding of turbulence is yet to be developed. Nevertheless, it has fascinated people across the centuries appearing in various pieces of artwork. Van Gogh's famous starry night captures stars at the night sky as whirling eddies of light that seem to flow over the painting. A comparison between eddies in starry night and measurements of turbulence in star formation found a surprising similarity between the luminosity wavenumber spectrum in these two datasets [33][1].
The motion of neutral fluids with mass density ρ, flow velocity $\mathbf{u}$ and viscosity η are described by the Navier-Stokes equations

$$\rho \left(\partial_t + (\mathbf{u} \cdot \nabla)\right) \mathbf{u} = -\nabla p + \eta \Delta \mathbf{u}. \tag{3.1}$$

The above equation can be understood from momentum conservation. The left hand side represents mass density times acceleration. The right hand side consists of a

[1] It is worth noting that the authors found the turbulent cascade in most paintings of van Gogh's 'turbulent period' but not in his other work. This is the same period where van Gogh famously cut off his ear. He seemingly grasped the nature of turbulence for a short period in his life

Figure 3.1: Van Goghs starry night. Light is depicted by very distinct, broad brushstrokes capturing its flickering motion on the night sky. Stars are whirling eddies. Only paintings from van Goghs era of psychotic agitation are shown to possess luminosity characteristics similar to nature [33]. Digital version provided by the New York metropolitan museum of modern arts [34].

pressure term and the internal resistivity of the fluid. Fluid flows show very distinct behaviour depending on the scale and flow velocity of the system. Equation 3.1 can be normalized to the typical length scale L, the typical flow velocity U and the corresponding time scale $T = L/U$ to obtain dimensionless equations

$$\mathbf{u}' = \frac{\mathbf{u}}{U}, \quad t' = \frac{t}{T}, \quad p' = \frac{pT^2}{\rho L^2},$$
$$\Rightarrow \left(\partial_{t'} + (\mathbf{u}' \cdot \nabla')\right) \mathbf{u}' = \nabla' p' + \frac{1}{\mathrm{Re}} \Delta' \mathbf{u}'. \tag{3.2}$$

The control parameter of this equation is the Reynolds number Re determining the regime of the fluid flow. It can be understood as the ratio between the non-linear term and the viscous friction term in equation 3.1.

$$\frac{\rho \left(\mathbf{u} \cdot \nabla\right) \mathbf{u}}{\eta \Delta \mathbf{u}} \sim \frac{\rho U L}{\eta} = \mathrm{Re}. \tag{3.3}$$

The former term is quadratic in the flow velocity and transports energy between the scales while the latter dissipates energy out of the system into the random field. A low Reynolds number is associated with quiescent, laminar flow without the creation of eddies. Systems with higher Reynolds numbers show irregular, turbulent behaviour. The difference of flows around a cylinder with varying Reynolds numbers is shown in figure 3.2.

3.2 Plasma Turbulence

Plasmas in magnetic fusion experiments are subject to turbulence as well as neutral fluids are. However, a plasma encompasses at least two particle species - electrons

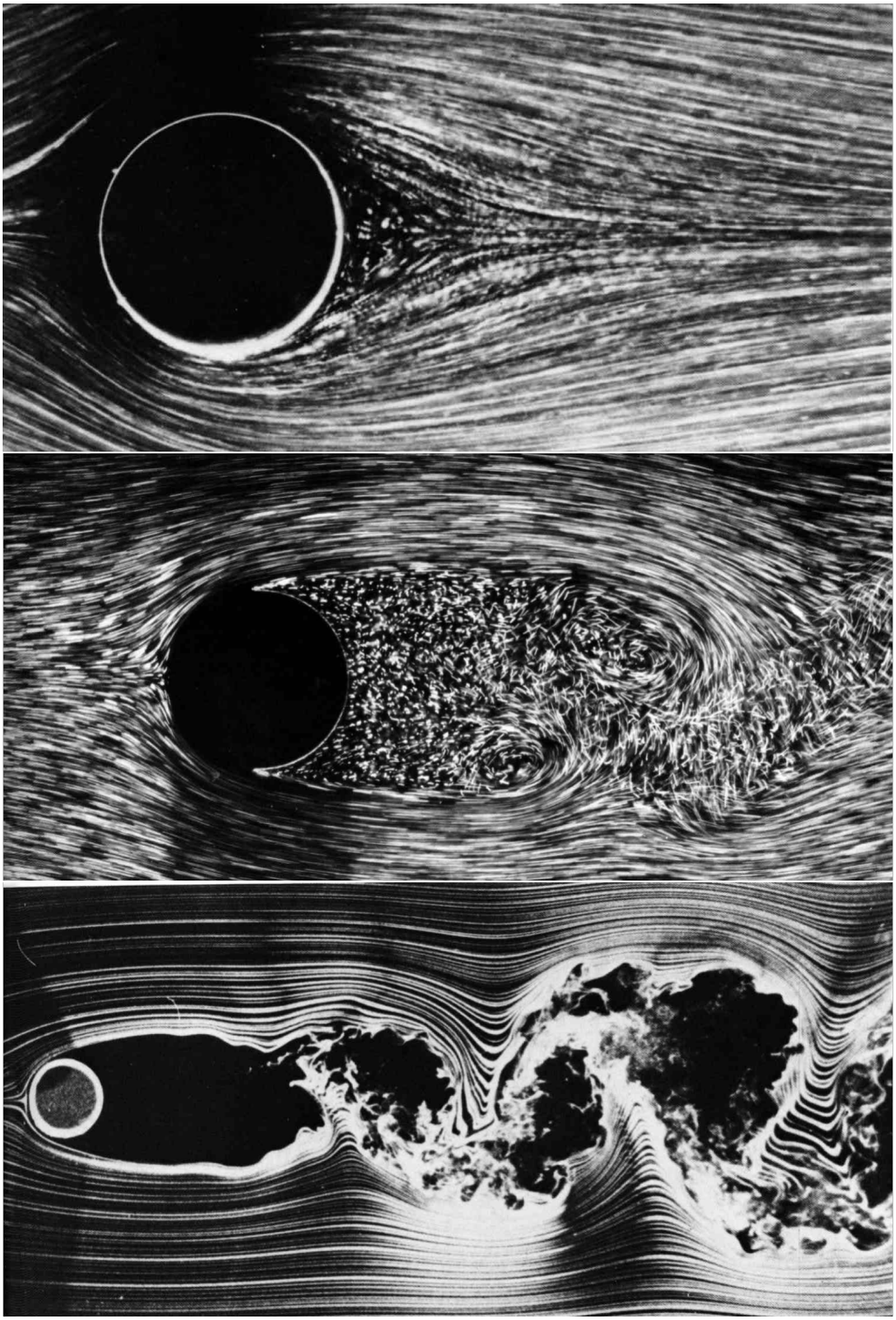

Figure 3.2: A flow around a solid cylinder at different Reynolds numbers (Re = 9.6, 2000, 10000 from top to bottom). At low Reynolds numbers the viscosity dominates and the flow is laminar. Higher Reynolds numbers cause increasingly stronger eddie formation and irregular behaviour. Pictures from [35].

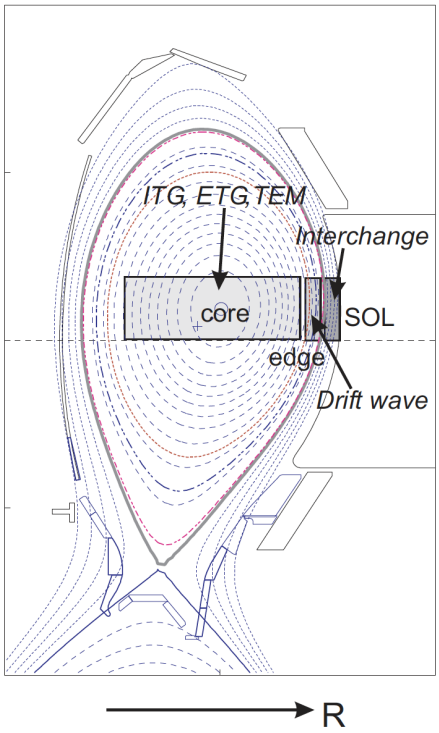

Figure 3.3: Different turbulence regimes in a tokamak. The turbulence in the core is mostly driven from electron and ion temperature gradients as well as trapped electrons. In the scrape-off layer the transport from filamentary structures dominates. Their advection is driven by a charge separation induced from the curvature. This is called interchange drive. Figure from [36].

and ions - with two different pressures p_e, p_i which are subject to electromagnetic forces given by the potentials ϕ and ψ. The density n of the two species is identical due to quasineutrality. Turbulent fluctuations occur in all quantities and there are transfer channels between all of them. In neutral fluid turbulence usually only the flow field $\mathbf{u}$ is of interest. Plasma turbulence needs to take into account all the different fields and their interplay.
There are several distinct regimes of plasma turbulence in a fusion relevant toroidal experiment. In the core the temperature is very high ($\sim 1...10\,\mathrm{keV}$). Particles experience very few collisions. This enables non-Maxwellian velocity distribution functions to persist which requires a kinetic treatment. Plasma dynamics in the core are usually described by kinetic and gyrokinetic models derived from equation 2.3 and its gyroaverage. At the edge of the confined region of the plasma steep temperature and density gradients fall off within only a few centimeters around the last closed flux surface. Further out the field lines are no longer closed around the torus but intersect the wall of the vacuum chamber forming the scrape-off layer (SOL). In the edge and SOL temperatures become lower and collisionalities higher enabling a fluid approach. A plasma in this parameter regime can be described with equations similar to the Navier-Stokes equations for neutral fluids. Similar to neutral fluids turbulence in plasma physics taps the free energy in the pressure gradients. In fusion experiments the gradient of the ion temperature (ITG) gives a strong contribution to particle and heat transport [37][38]. Similar to the propagation of filaments discussed below a background pressure gradient parallel to the curvature vector of the

magnetic field leads to a finite divergence of the diamagnetic current creating charge separation and radial transport due to the resulting $\mathbf{E} \times \mathbf{B}$ drift.

3.3 Filaments in the Scrape-off Layer

Beyond the last closed flux surface gradients are weak and the turbulence is driven by transport due to coherent structures expelled from the confined region. Coherent structures in the SOL of fusion plasmas are called filaments or blobs. These coherent plasma structures have a size on the order of one centimeter perpendicular to the magnetic field. Blobs are typically aligned to the background magnetic field $\mathbf{B}$ and advected radially outwards. They are emitted and propagate a distance several times their own diameter transporting heat and particles from the edge into the SOL to drive turbulent dynamics in this region. This process is known as turbulence spreading and has been observed e.g. in the COMPASS tokamak [39]. Turbulence

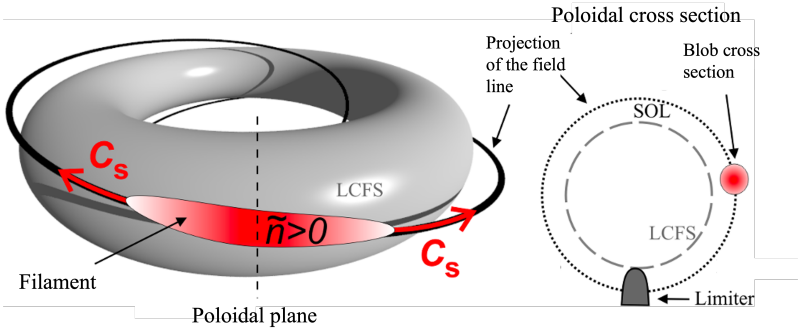

Figure 3.4: 3-dimensional image of a blob along a field line on the outboard side of a tokamak (left) and poloidal crosssection of the blob (right) [40].

in the SOL is therefore dependent on edge dynamics but can vice versa influence this region. The interplay between these two different regimes of plasma dynamics is beyond the scope of this thesis. Simulations in the following chapters initialize a plasma blob on an open field line in the SOL and investigate its propagation. It features a monopole density perturbation with a maximum of several times the background density providing a loss channel for heat and particle transport in toroidal confinement devices [41].

3.4 Propagation Mechanism of Filaments

In this section the basic mechanism of filamentary transport is introduced. A pressure perturbation and the curvature or gradient of the magnetic field lead to a finite divergence of the diamagnetic current and a charge separation creating a potential dipole. The resulting electric field advects the pressure perturbation radially outwards via the $\mathbf{E} \times \mathbf{B}$ drift. This is the fundamental mechanism driving filament motion. The charge accumulation drives currents to ensure the quasineutrality condition $\nabla \cdot \mathbf{j} = 0$. The currents reduce the potential dipole limiting the drive for propagation.
The dipole potential can be resolved either perpendicular to the magnetic field via

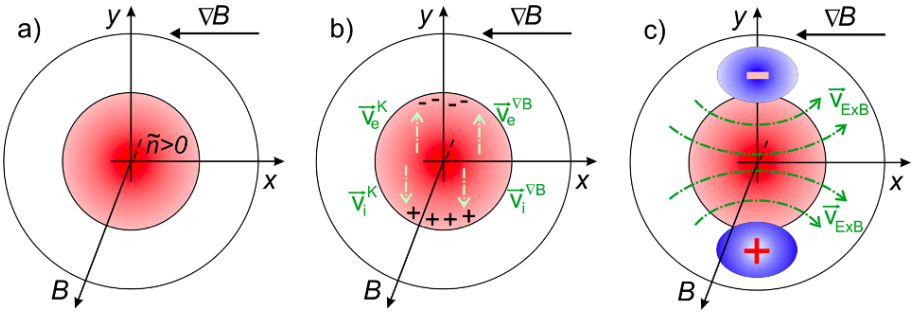

Figure 3.5: Basic mechanism of filament motion. A positive density perturbation (left) on the outboard size of a tokamak causes a charge separation (middle) which leads to a radial $\mathbf{E} \times \mathbf{B}$ advection of the density perturbation (right) [40].

the polarization current or via parallel currents if the filament intersects the wall. As the electron flow onto wall elements is larger than the ion flow, the sheath - a conductive layer - develops, connecting the two parts of the dipole [42]. The potential dissipation determines the propagation regime of the filament. These different regimes will be discussed in section 3.5

Simple blob models usually rely on the cold ion assumption ($T_i = 0$) [24][43]. This is not consistent with experimental findings in the SOL of e.g. ASDEX Upgrade (AUG). Ion temperatures are 2-3 times higher than electron temperatures [44]. A strong ion pressure perturbation creates a contribution to the potential via the ion polarization current in the vorticity in equation 2.21. This has been shown in simulations [45]. In `hermes-2` the electrostatic potential ϕ is determined by inverting the vorticity definition. The perpendicular Laplace operator needs to be inverted numerically. This is indicated by $\nabla_\perp^{-2}$. The equation to calculate the potential then reads

$$\phi = \frac{1}{n_0}\left(B^2 \nabla_\perp^{-2} \omega - p_i\right). \tag{3.4}$$

If the ion pressure contribution dominates, the potential becomes monopolar. The corresponding $\mathbf{E} \times \mathbf{B}$ drift leads to a rotating motion If the monopole and dipole part of the potential are of similar size the rotation leads to a significant part of the filament advection being in poloidal direction as illustrated in Figure 3.6.

Knowing the basic mechanisms of filament motion analytical scaling laws for the velocities can be derived in the next section. Different scaling regimes arise for each dominant mechanism of the potential dissipation. These are the polarization current for hot and cold ions and the parallel current.

3.5 Velocity Scalings

Quantitative scaling laws for filaments can be obtained by applying the blob correspondence principle [18] [41]. Gradient and time derivative operators are replaced by average blob quantities. Perpendicular gradients are assumed to scale as $\delta_\perp^{-1}$ with $\delta_\perp$ being the perpendicular diameter of the filament. The typical blob velocity is v_b and the corresponding timescale is $\tau_b = \delta_\perp / v_b$. The expression for the perpendicular potential gradient $\nabla_\perp \phi$ assumes the $\mathbf{E} \times \mathbf{B}$ drift to be the dominant part of the blob

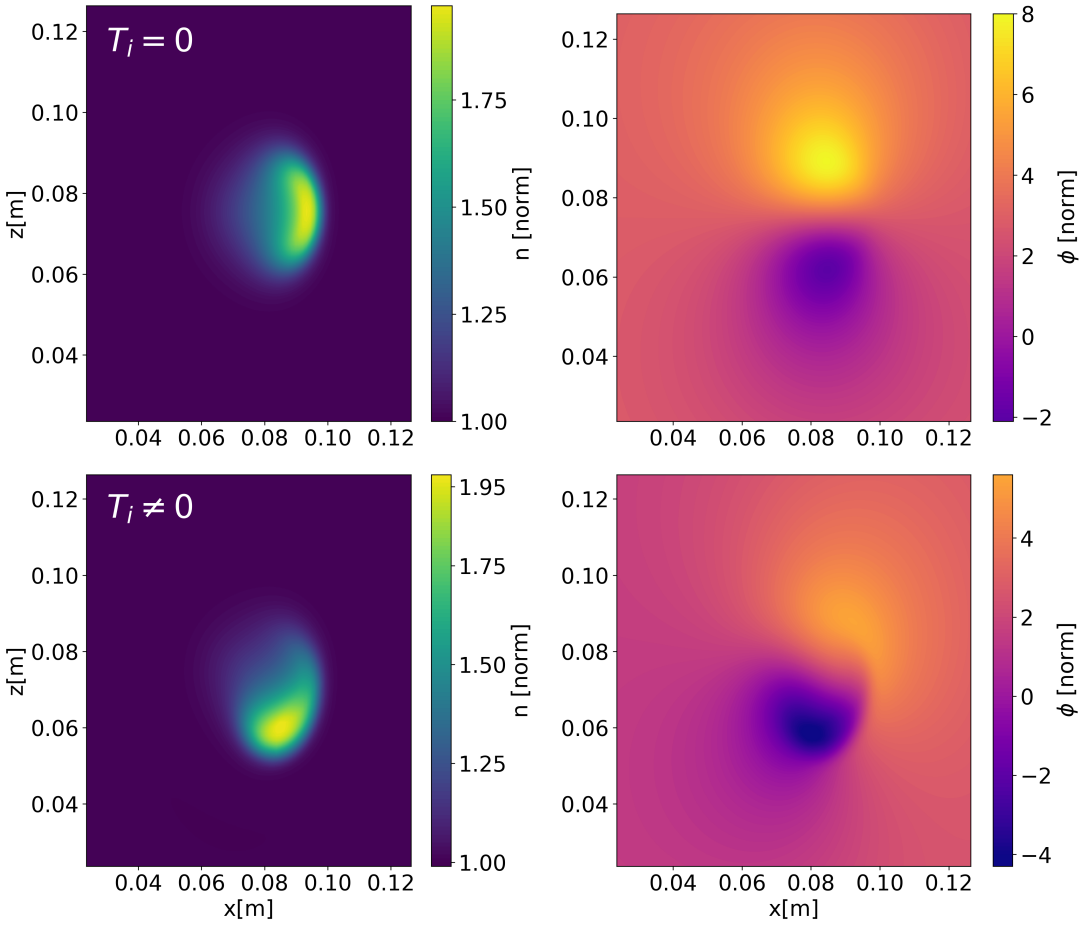

Figure 3.6: Propagation of a blob with cold (top) and hot ions (bottom). The pictures on the left show the relative density. On the right the normalized potential $e\phi/T$ is displayed. Hot ions lead to a monopole contribution to the potential (bottom right). The trajectory of the filament gets tilted (bottom left). The axis x and z denote the normal (radial) and binormal (poloidal) direction with respect to the magnetic field.

velocity

$$\nabla_\perp \to \frac{i}{\delta_\perp}, \quad \partial_t \to \frac{i\delta_\perp}{v_b}, \quad \nabla_\perp \phi \to v_b B. \tag{3.5}$$

This is used to rewrite the vorticity equation 2.22 in terms of these characteristic quantities. Only the terms related to the divergence of the ion polarization, diamagnetic and parallel currents are considered. These are behind the primary mechanisms of blob propagation. The higher order terms in the ion polarization current as well as cross-field and parallel viscosity are neglected. The simplified vorticity equation reads

$$\partial_t \left(\nabla \cdot \left[\frac{1}{B^2} \left(n_0 \nabla_\perp \phi + \nabla_\perp p_i \right) \right] \right) = \nabla \cdot \left(\left(p_e + p_i \right) \nabla \times \frac{\mathbf{b}}{B} \right) + \nabla_\parallel j_\parallel. \tag{3.6}$$

The ion polarization current on the RHS of the above equation contains a contribution from the ion pressure as explained in section 3.4. The ratio between ion

and electron temperature is τ_i. Applying the relations from 3.5 and discarding the parallel current leads to

$$-\frac{v_b}{B^2\delta_\perp^2}\left(-n_0 v_b B + \frac{i}{\delta_\perp}\tau_i p_e\right) = -\frac{2i}{B\delta_\perp}\left(1+\tau_i\right)\kappa\, p_e \tag{3.7}$$
$$\Leftrightarrow \left(v_b - i\frac{\tau_i}{2\delta_\perp n_0 B}p_e\right)^2 = -\left(\frac{\tau_i}{2\delta_\perp n B}p_e\right)^2 - i\frac{2\delta_\perp B}{n_0}\left(1+\tau_i\right)\kappa\, p_e.$$

The expression for the curvature is simplified as $\nabla\times\mathbf{b}/B \approx 2/B\ (\mathbf{b}\times\kappa) \sim 2\kappa/B$ if only a constant curvature perpendicular to the magnetic field is considered. The case of inhomogeneous curvature is discussed in the following section. The above equation can be abbreviated

$$\left(v_b - i\sqrt{f}\right) = -f - ig. \tag{3.8}$$

f determines the contribution of the ion pressure perturbation to the potential while the curvature drive is captured in g. These two terms read

$$f = \left(\frac{\tau_i}{2\delta_\perp n_0 B}p_e\right)^2 \tag{3.9}$$
$$g = \frac{2\delta_\perp B}{n_0}\left(1+\tau_i\right)\kappa\, p_e.$$

Multiplying with the complex conjugate and solving for v_b gives

$$|v_b| = \sqrt{\sqrt{f^2+g^2} - f}. \tag{3.10}$$

Neglecting hot ion terms ($g \gg f$) the conventional inertial scaling for blob velocity is obtained

$$|v_b| = \left(\frac{2p_e\delta_\perp}{n_0}\kappa\right)^{\frac{1}{2}}. \tag{3.11}$$

If the hot ion contribution in the polarization is dominating ($f \gg g$) the blob is in the ion pressure dominated inertial regime. Its velocity scales as follows after taylor expanding the inner square root

$$|v_b| = \sqrt{f\sqrt{1+\frac{g^2}{f^2}} - f} \approx \sqrt{f\left(1+\frac{g^2}{2f^2}\right) - f} = \frac{1}{2}\sqrt{\frac{g^2}{f}} = 2\frac{(1+\tau_i)}{\tau_i}B\delta_\perp^2\kappa. \tag{3.12}$$

If the parallel current dominates the velocity scales as $\delta_\perp^{-2}$. Depending on the regime the parallel current is either limited by sheath resistance, ohmic resistance or electromagnetic inductance. Assuming for simplicity the first order sheath closure model $1/e\,\nabla_\parallel j_\parallel = n\phi/L_\parallel$ [46] and neglecting both inertial and hot ion contributions in equation 3.6 gives the Krashenninikov [17] scaling for sheath limited filaments with an additional factor of $(1+\tau_i)$ to include the finite ion temperature

$$|v_b| = \frac{2L_\parallel}{\delta_\perp^2}\left(1+\tau_i\right)\kappa\, p_e. \tag{3.13}$$

The calculations in this section have been performed analogously for the DALF model [47]. Similarly to `hermes-2` it describes physics in the edge and SOL by

means of fluid equations. In contrast, it employs a different ordering and therefore it includes different effects, namely MHD and interchange dynamics. DALF only evolves the fluctuations, not the background of quantities.
Three different scalings of the velocity with the perpendicular blob size $\delta_\perp$ were derived in this section. If the parallel current $j_\parallel$ dominates over the polarization current the velocity scales as $\delta_\perp^{-2}$. If the ion pressure contribution to the polarization dominates a scaling of $v_b \sim \delta_\perp^2$ is found. If the polarization current dominates and the ions are cold the velocity scales as $\delta_\perp^{1/2}$. All scaling laws assume a constant curvature and parallel homogeneous filaments. The following chapters introduce parallel curvature variations which modify the filament drive as well as the dynamics of the parallel current. It is investigated how these parallel inhomogeneities influence the blob motion.

3.6 Varying Curvature

The curved nature of magnetic field lines in tokamaks and stellarators drives blob propagation. More precisely it is determined by the divergence of the diamagnetic current. It can be rewritten as

$$\begin{aligned} \nabla \cdot \mathbf{j}_{dia} = \nabla \cdot \left(\frac{\mathbf{b} \times \nabla p}{B} \right) &= \left(\nabla \times \frac{\mathbf{b}}{B} \right) \cdot \nabla p \\ &= \left(\frac{2}{B} \mathbf{b} \times \kappa + \frac{2}{B^2} \mathbf{b} \times \nabla B \right) \cdot \nabla p. \end{aligned} \tag{3.14}$$

where $\kappa = \mathbf{b} \cdot \nabla \mathbf{b} = \mathbf{b} \times (\nabla \times \mathbf{b})$ is the magnetic curvature [48]. A pressure gradient parallel to $\mathbf{b} \times \kappa$ or $\mathbf{b} \times \nabla B$ leads to a charge accumulation due to a finite divergence of the perpendicular current. A magnetic field gradient is linked to the curvature via [49]

$$\begin{aligned} \kappa = \mathbf{b} \times \left(\nabla \times \frac{\mathbf{B}}{B} \right) &= -\mathbf{b} \times \frac{\mu_0 \mathbf{j} + \mathbf{b} \times \nabla B}{B} \\ &= \frac{\mu_0 \nabla p}{B^2} + \frac{\nabla_\perp B}{B}. \end{aligned} \tag{3.15}$$

In this thesis the perpendicular gradient in the magnetic field is neglected as it is assumed to vary only weakly on the perpendicular scale of the simulation domain of only 0.1 m.
. The curvature of a magnetic field line can be split up into its normal and geodesic components. The normal curvature κ_n quantifies to which extent the curvature vector is normal to the flux surface

$$\kappa_n = \mathbf{n} \cdot \kappa. \tag{3.16}$$

The vector $\mathbf{n}$ is the normal vector of the flux surface. The geodesic curvature κ_g describes the part of the curvature tangential to the flux surface

$$\kappa_g = (\mathbf{n} \times \mathbf{b}) \cdot \kappa. \tag{3.17}$$

The total curvature is given by $\kappa^2 = \kappa_g^2 + \kappa_n^2$ [49]. In toroidal magnetic confinement devices the radial magnetic field vanishes. To illustrate the curvature of twisted

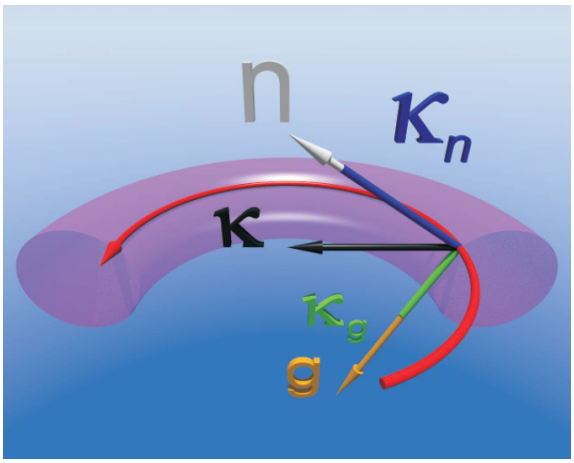

Figure 3.7: The normal and geodesic curvature components for a helical magnetic field line [50]. The normal curvature is the scalar product of κ and $\mathbf{n}$. The geodesic curvature is the scalar product of the curvature with the tangential vector of the flux surface ($\mathbf{n} \times \mathbf{b}$) which is denoted here as $\mathbf{g}$

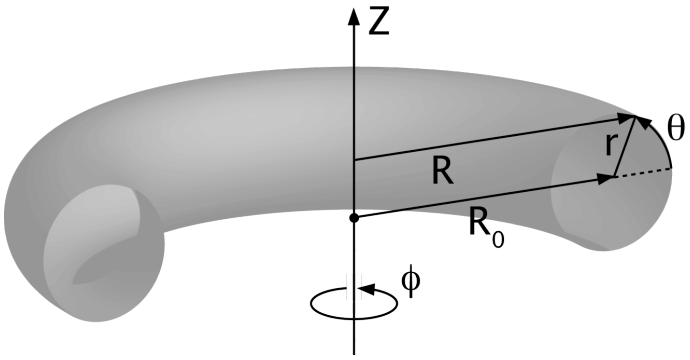

Figure 3.8: An illustration of the toroidal coordinate system used in this section [51]. r denotes the radial component originating from the center of the poloidal cross section. The poloidal and toroidal angles are given by θ and ϕ. Looking from above ϕ runs counterclockwise.

magnetic field lines in a toroidal geometry the curvature of a simple tokamak with circular cross section is calculated. Naturally, torus coordinates (r, ϕ, θ) are used. The radial component is with respect to the center of the cross section of the torus while ϕ and θ denote toroidal and poloidal angles. Its major and minor radii are R_0 and a respectively. The safety factor $q = B_\phi a / B_\theta R_0$ indicates how often a field line turns around the torus toroidally while performing one poloidal turn. The transformation between cartesian (x, y, z) and torus coordinates (r, ϕ, θ) reads

$$\begin{aligned} x &= (R_0 + r\cos(\theta))\cos(\phi) \\ y &= s_\phi\,(R_0 + r\cos(\theta))\cos(\phi) \\ z &= s_\theta\, r \sin(\theta) \end{aligned} \tag{3.18}$$

There are two additional factors s_ϕ and s_θ. The natural choice is $s_\phi = s_\theta = 1$. However, in this case the coordinate system is left-handed. To achieve a right-handed coordinate system the poloidal direction is reversed so $s_\phi = 1$ and $s_\theta = -1$. The

basis vectors can be constructed via $e_i = \partial_i \mathbf{r}$ with the position vector $\mathbf{r} = (x, y, z)^{\mathrm{T}}$

$$\begin{aligned}
\hat{\mathbf{e}}_\mathbf{r} &= \frac{\partial \mathbf{r}}{\partial r} = \begin{pmatrix} \cos(\theta)\cos(\phi) \\ \cos(\theta)\sin(\phi) \\ -\sin(\theta) \end{pmatrix}, \\
\hat{\mathbf{e}}_\phi &= \begin{pmatrix} -\left(R_0 + r\cos(\theta)\right)\sin(\phi) \\ \left(R_0 + r\cos(\theta)\right)\cos(\phi) \\ 0 \end{pmatrix}, \\
\hat{\mathbf{e}}_\theta &= \begin{pmatrix} -r\sin(\theta)\cos(\phi) \\ -r\sin(\theta)\sin(\phi) \\ -r\cos(\theta) \end{pmatrix}.
\end{aligned} \tag{3.19}$$

From the basis vectors the metric tensor $g_{ij} = \hat{\mathbf{e}}_\mathbf{i} \cdot \hat{\mathbf{e}}_\mathbf{j}$ is calculated. As the basis vectors are orthogonal the metric tensor becomes diagonal.

$$g = \begin{pmatrix} 1 & 0 & 0 \\ 0 & \left(R_0 + r\cos(\theta)\right)^2 & 0 \\ 0 & 0 & r^2 \end{pmatrix} \tag{3.20}$$

The vacuum magnetic field vector, the unit vector and the field strength of a circular tokamak in toroidal and poloidal coordinates read [52]

$$\begin{aligned}
\mathbf{B} &= B_0 \begin{pmatrix} 0 \\ 1 - \frac{r}{R_0}\cos(\theta) \\ \frac{r}{qR_0}\left(1 - \frac{r}{R_0}\cos(\theta)\right) \end{pmatrix}, \quad \mathbf{b} = \frac{1}{\sqrt{1 + \left(r/qR_0\right)^2}} \begin{pmatrix} 0 \\ 1 \\ \frac{r}{qR_0} \end{pmatrix}, \\
B &= B_0 \left(1 - \frac{r}{R_0}\cos(\theta)\right)\sqrt{1 + \left(\frac{r}{qR_0}\right)^2}.
\end{aligned} \tag{3.21}$$

The curvature $\kappa = \mathbf{b} \cdot \nabla \mathbf{b}$ is expressed for orthogonal coordinates [53]

$$\left(\mathbf{b} \cdot \nabla \mathbf{b}\right)_i = \sum_k \left[\frac{b_k}{\sqrt{g_{kk}}} \frac{\partial b_i}{\partial x_k} + \frac{b_k}{\sqrt{g_{kk} g_{ii}}} \left(b_i \frac{\partial \sqrt{g_{ii}}}{\partial x_k} - b_k \frac{\partial \sqrt{g_{kk}}}{\partial x_i} \right) \right]. \tag{3.22}$$

Inserting the expressions for the magnetic field from equation 3.21 one obtains

$$\kappa = \frac{1}{1 + \left(\frac{r}{qR_0}\right)^2} \begin{pmatrix} -\frac{r}{q^2 R_0^2} - \frac{\cos(\theta)}{R_0 + r\cos(\theta)} \\ -\frac{r\sin(\theta)}{qR_0(R_0 + r\cos(\theta))} \\ \frac{\sin(\theta)}{R_0 + r\cos(\theta)} \end{pmatrix} \tag{3.23}$$

For a circular tokamak the normal vector on the flux surfaces is $\mathbf{n} = (1, 0, 0)^{\mathrm{T}}$. The tangential vector reads

$$\mathbf{n} \times \mathbf{b} = \frac{1}{\sqrt{1 + \left(\frac{r}{qR_0}\right)^2}} \begin{pmatrix} 0 \\ -\frac{r}{qR_0} \\ 1 \end{pmatrix}. \tag{3.24}$$

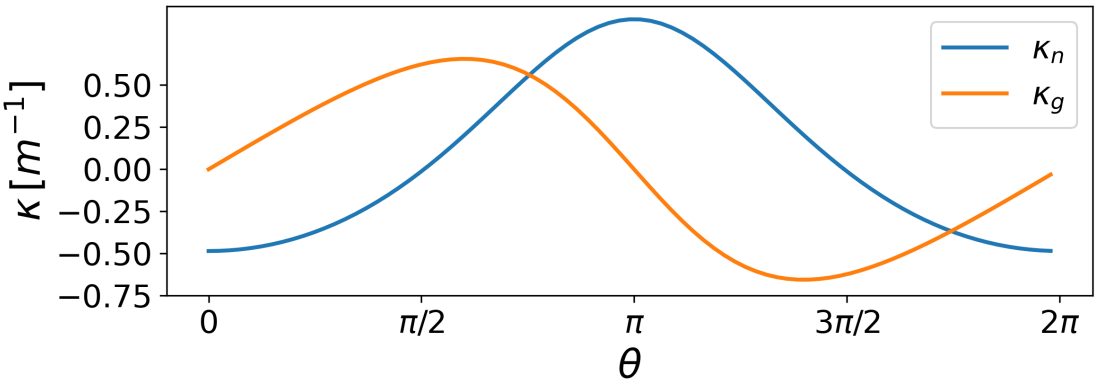

Figure 3.9: Normal and geodesic curvature for a circular tokamak with AUG parameters (R_0 =1.6 m, r=0.5 m, q=4). Normal curvature is minimal for the outboard side ($\theta = 0$) of the tokamak and maximal on the inboard side ($\theta = \pi$). Geodesic curvature is highest on the upper side ($\theta = \pi/2$) on the tokamak while being minimal on the lower side ($\theta = 3\pi/2$).

Following equations 3.16 and 3.17 the geodesic and normal curvature components can be calculated

$$\kappa_n = \kappa \cdot \mathbf{n} = -\frac{1}{1+\left(\frac{r}{qR_0}\right)^2}\left(\frac{r}{q^2R_0^2} + \frac{\cos(\theta)}{R_0 + r\cos(\theta)}\right), \tag{3.25}$$

$$\kappa_g = \kappa \cdot (\mathbf{n} \times \mathbf{b}) = \frac{1}{\sqrt{1+\left(\frac{r}{qR_0}\right)^2}}\frac{\sin(\theta)}{R_0 + r\cos(\theta)}.$$

In the limit of large aspect ratios ($R \gg a$) this simplifies to

$$\kappa_n = -\frac{\cos(\theta)}{R_0}, \quad \kappa_g = \frac{\sin(\theta)}{R_0}. \tag{3.26}$$

The curvature for any helical magnetic field line is not homogeneous. Parallel variations in the curvature lead to a modified polarization as the divergence of the diamagnetic current varies along the field line. The curvature of a circular tokamak is calculated in this section. The curvature of a stellarator is more complicated due to the non axisymmetric magnetic field. The curvature of a W7-X fieldline is displayed in figure 3.10. It features regions of negative curvature and sharp localized spikes of high curvature. The next section investigates the parallel dynamics which determine the currents resolving the parallel potential gradient.

3.7 Parallel Dynamics

Inhomogeneous polarization in a filament along a field line is driven by the parallel varying curvature κ. This leads to a parallel potential gradient $\partial_\parallel \phi$ which causes a response of the parallel current. Neglecting the parallel momentum contributions due to the m_e/m_i prefactor in equation 2.29 a simplified version of Ohms law is obtained

$$\partial_\parallel \phi = \frac{1}{2}\beta_e \partial_t \psi - \frac{\nu}{n} j_\parallel + \frac{1}{n}\partial_\parallel p_e + 0.71 \partial_\parallel T_e. \tag{3.27}$$

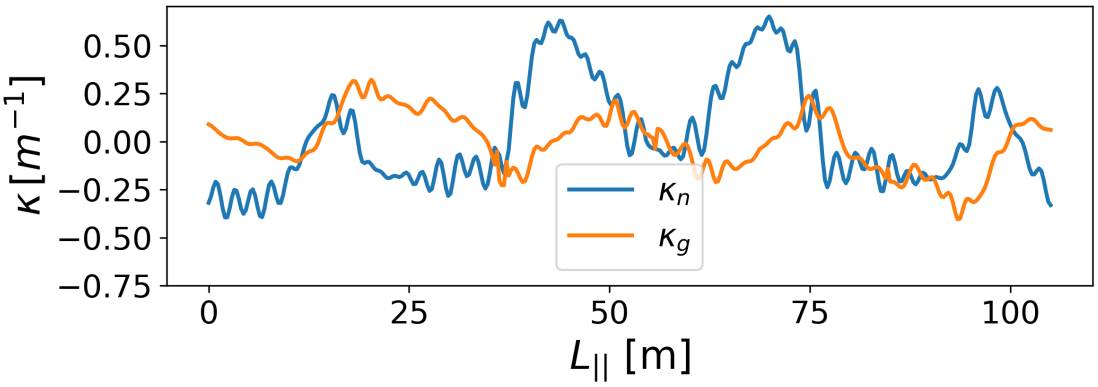

Figure 3.10: Normal and geodesic curvature of a field line in W7-X. The stellarator magnetic field possesses regions of negative normal curvature as well as sharp localized spikes. This field line crosses the line of sight of a Gas Puff Imaging diagnostic in W7-X. Field line data from IPP-Webservices [54].

A parallel potential gradient $\partial_\parallel \phi$ drives parallel currents $j_\parallel$ which are limited by Ohmic resistance determined by collisionality $\frac{\nu}{n} j_\parallel$ and the inductance term $\beta_e \partial_t \psi / 2$. Both terms increase the propagation time of the parallel current which has been confirmed in analytical and numerical work on cold-ion blob cases [55] [56] [57]. Usually, it is assumed that blobs are homogeneous along a field line [41]. A long propagation time of the parallel current defies this assumption.
The mechanism that determines the parallel coherence of a turbulent structure can be summarized as follows: A pressure perturbation is aligned to a field line with parallel varying curvature. It experiences an inhomogeneous polarization from the varying and finite divergence of the diamagnetic current. The strength of the charge separation along a field line varies due to differing polarization resulting from varying curvature. This leads to differential $\mathbf{E} \times \mathbf{B}$ drift between different toroidal positions. The parallel potential gradient drives parallel currents which are limited by Ohmic resistance and inductance. A schematic view of a filament and its current balance is shown in figure 3.11. Two competing timescales arise: The blob advection time and the propagation time of the parallel current. If the local $\mathbf{E} \times \mathbf{B}$ drift pushes the filament apart faster than the parallel current flattens the parallel potential gradient, the structure is ripped apart. If the parallel current is strong enough the blob will remain coherent. This leads to the main research question of this work: For which parameters regimes does a parallel variation in the curvature decorrelate the filaments along the field line?

3.8 Filaments in Stellarators

Filaments are a well known channel of particle and heat loss in tokamaks [41]. Extensive experimental and numerical studies have been performed to validate the propagation models described in section 3.5 [47]. Measurements of blob densities and temperatures have been taken via various methods [44][58][59]. The database on turbulence in stellarators is small compared to tokamaks as there are fewer machines. The dipole polarization of a poloidal pressure perturbation is observed via a phase shift between floating potential and ion saturation current measurements

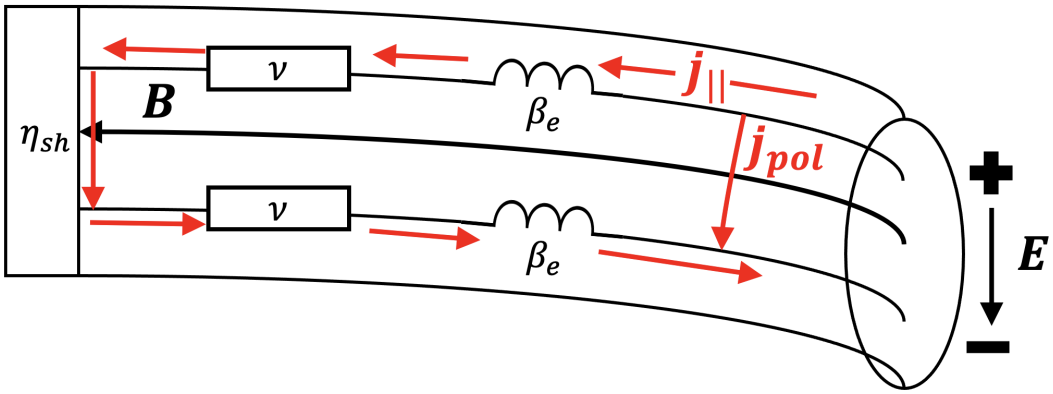

Figure 3.11: The current balance of a filament in an equivalent circuit analogous to [18]. The potential dipole is resolved perpendicular to the magnetic field via the polarization current and the parallel current. The parallel current is limited by the sheath resistance η_{sh}, the Ohmic resistance ν and electromagnetic induction. Ohmic resistance is controlled by the collisionallity $\ni$. Inductance is controlled by the electron plasma beta β_e.

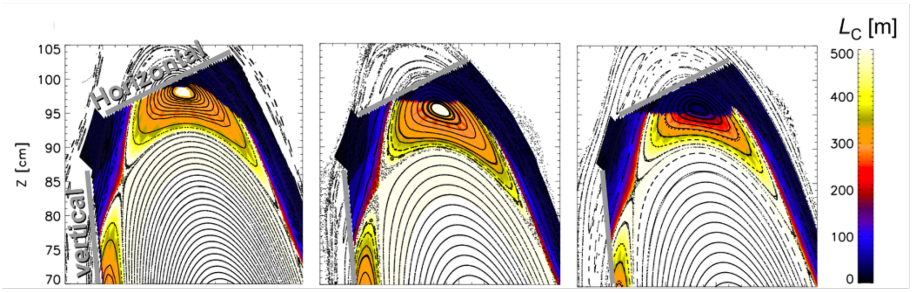

Figure 3.12: Parallel connection length in W7-X for different magnetic configurations. The island divertor leads to highly varying $L_{||}$ profiles [65].

e.g in W7-AS [60]. Filamentary field-aligned structures which are connected to the sheath have been observed in the stellarators W7-AS and TJ-K [61][62][63]. In TJ-K blobs contribute as much as 30% of the total particle transport in the SOL and show a poloidal velocity component originating of a polarization via the geodesic curvature [62]. Poloidal propagation has also been observed in W7-AS and LHD which is found to be triggered by a finite radial shear of the magnetic field [63][64]. Experimental investigations with Langmuir probes found filamentary structures in W7-X to propagate slowly in radial direction due to the large major radius compared to AUG ($R_{maj} = 6\,\mathrm{m}$ vs. $2.5\,\mathrm{m}$ with similar minor radius of $0.5\,\mathrm{m}$). Scalings of the velocity with the perpendicular blob size show quantitative agreement despite neglecting the inhomogeneous curvature drive [66]. The island divertor of W7-X produces a highly varying profile of the parallel connection length as illustrated in figure 3.12. It determines the magnitude of the parallel current and the propagation regime of the filament. Numerical studies suggest that this leads to blobs changing their propagation regime provided they are still coherent enough by the time they propagate into the region of the aprupt change of the parallel connection length

$L_\parallel$ [67]. The question of filament coherence for varying curvature has been tackled with cold filaments for pellet relevant conditions [68]. A non-uniform propagation is caused by non-uniform curvature drive. An increase in temperature is shown to lead to more coherent filaments. Filaments seem to propagate slower compared to tokamaks. Parallel varying curvature could decorrelate coherent structures along a fieldline.
The following chapters investigate the influence of varying curvature on filaments for sinusoidal, tokamak and stellarator cases as well as the relevant parallel plasma dynamics by means of numerical simulations.

Chapter 4

Simulation Setup and Benchmarks

This chapter starts with a description of the BOUT++ numerical framework which is used to simulate the hermes-2 model equations described in section 2.3. In section 4.2 the numerical methods used specifically in this thesis are briefly discussed. Section 4.3 lists the initial conditions used for the simulations in this thesis. Section 4.4 reproduces the different scalings of filaments velocity with the blob size for hot and cold ion cases.

4.1 The BOUT++ Framework

BOUT++ is a framework to simulate nonlinear differential equations for plasmas and fluids in curvilinear coordinates [69][70]. It is used to simulate a variety of different physics models. Those include resistive MHD models [71], neutral physics investigating nitrogen seeding [72] and the physics of filaments in the SOL [67][73]. Its main design aim is to decouple modeling and simulation of physical processes from numerical implementation. Differential operators have an intuitive nomenclature easing implementation. For instance, the common Hasegawa-Watakani model [74][75] for electrostatic drift wave turbulence[1]

$$\partial_t \tilde{n} + \{\tilde{n}, \tilde{\phi}\}_{x,z} = -\kappa \frac{\partial \tilde{\phi}}{\partial z} + \hat{C}(\tilde{n} - \tilde{\phi}) \tag{4.1}$$

$$\partial_t \omega + \{\omega, \tilde{\phi}\}_{x,z} = \hat{C}(\tilde{n} - \tilde{\phi}) \tag{4.2}$$

reads in BOUT++ syntax

```
ddt(n) = -bracket(phi, n) - kappa*DDZ(phi) + C*(phi - n);
ddt(vort) = -bracket(phi, vort) + C*(phi - n);
```

In this model $\tilde{n}$ and $\tilde{\phi}$ denote density and potential fluctuations. The control parameters are the parallel coupling strength $\hat{C}$ and the inverse fall-off length of the background density gradient $\kappa = 1/L_n = |\nabla n_0/n_0|$.
In the following chapters the BOUT++ framework is used to simulate the hermes-2 model equations. The next two sections describe the specific numerical methods and initial conditions used during this work.

[1] $\{...\}_{i,j}$ refers to the Poisson brackets with $\{f, g\}_{i,j} = (\partial_i f)(\partial_j g) - (\partial_j f)(\partial_i g)$

4.2 Differential Operators

The fluid equations used in this thesis contain first derivatives in time and up to third order spatial derivatives. All spatial derivatives are computed via 4-th order finite volume schemes. The electrostatic and parallel vector potential ϕ and ψ are computed via Laplacian inversion using `Petsc` [76][77][78]. All of these steps compute the right hand side (RHS) of the equations. Finally the time evolution is implemented via the ODE solver `PVODE` solving equations of the form

$$\frac{\mathrm{d}f}{\mathrm{d}t} = \mathrm{RHS}(f, \nabla^i f, g, \nabla^i g, ...). \tag{4.3}$$

In this thesis the coordinate system is designed as follows: The radial direction is labeled with x. y is the parallel coordinate and z is the binormal direction. The x-direction requires 2 guard cells on each side to calculate the finite volume derivatives. The z-direction has periodic boundary conditions by design.

4.3 Initial Conditions and Simulation Outputs

In this section the necessary initial conditions to the `hermes-2` model are presented to investigate the coherence of turbulent structures subject to inhomogeneous curvature. The simulations are performed on a rectangular grid with the number of grid points being $(n_x, n_y, n_z) = (132, 16, 128)$ in most cases. The corresponding grid spacing is $(dx, dy, dz = (L_\perp/(n_x - 4), L_\parallel/n_y, L_\perp/n_z)$. The perpendicular domain width $L_\perp$ was chosen to inset the cross section of the filament with a sufficient distance to the boundary. It is on the order of 0.1 m. $L_\parallel$ is the parallel connection length which is equivalent to the parallel domain width for open field lines. In the following chapters it ranges from 10 m to 200 m. At the parallel upper and lower boundary the dynamics of plasma interaction with the sheath have to be modeled. This thesis employs the Bohm sheath model

$$v_{\parallel,i} \geq c_s, \quad \partial_\parallel n = \partial_\parallel T_e = \partial_\parallel \phi = 0. \tag{4.4}$$

It assumes supersonic parallel ion flow $v_{\parallel,i}$ onto the sheath and zero gradients for the other fields.
Quantities in `hermes-2` are normalized to a reference density N, temperature T and magnetic field B which is fixed at 2.5 T. The parameters determining parallel dynamics are the electron plasma beta β_e and the collisionality ν. In the `hermes-2` model these parameters cannot be changed directly but have to be changed by modifying the above normalization parameters. Expressions for β_e and ν read

$$\beta_e = \frac{2\mu_0 NT}{B^2} \text{ and } \nu = \frac{1}{1.96\tau_e m_i/m_e} \tag{4.5}$$

where τ_e is the electron ion collision frequency

$$\tau_e = \frac{1}{2.91 \cdot 10^{-6}\,(N/10^6)\,\lambda_{e,i}\,T^{-3/2}}, \quad \lambda_{e,i} = 24 - \log(\sqrt{N/10^6}\,/\,T). \tag{4.6}$$

A filament is initialized as a Gaussian perturbation in the density and the electron and ion pressure fields perpendicular to the magnetic field. Initially it is homogeneous parallel to the magnetic field. The input parameters for a filament are

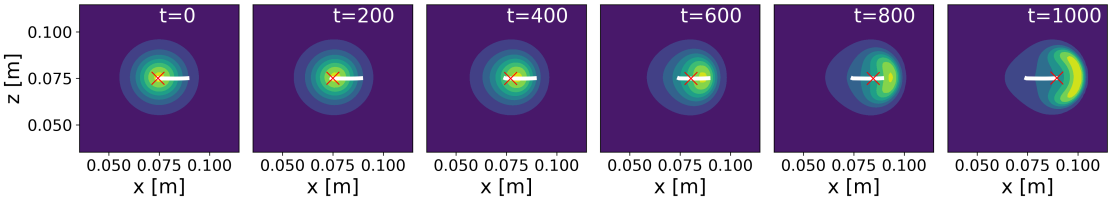

Figure 4.1: The COM of a filament is plotted onto the blob density distribution during its propagation at one poloidal plane. It is used as a measure for the position of the blob. The time is in units of $1/\omega_{c,i}$. The trajectory of the COM is indicated by the white line. The current position is marked by a cross.

the amplitude of the density and pressure perturbations as well as the blob size $\delta_\perp$. It represents the standard deviation of the Gaussian perturbation. The initial condition for the normalized density reads

$$n(x,y,z,t) = 1 + \sqrt{2\pi\delta_\perp^2}\sqrt{(2\pi)^3\,\delta_\perp^2}\,e^{-\frac{(x-0.5)^2}{2\delta_\perp^2}}\,e^{-\frac{(z-\pi)^2}{4\pi^2\delta_\perp^2}}. \tag{4.7}$$

In `BOUT++` the x direction is normalized to 1. z is normalized to 2π. This leads to the seemingly different standard deviations between the Gaussian distributions in x and z direction in the initial condition to create a symmetric blob. The simulation outputs are 4 dimensional arrays with axis (t,x,y,z) of size (t_{max},n_x,n_y,n_z) for each field. The position $\mathbf{r}(t_i,y_i)$ and perpendicular velocity $\mathbf{v}(t_i,y_i)$ of the center of mass (COM) of a filament for each poloidal plane is determined from the density field

$$\mathbf{r}(t_i,y_i) = \sum_{i,j}^{n_x,n_z} n_{i,j},\mathbf{r}_{i,j} \text{ and } \mathbf{v}(t_i,y_i) = \frac{\mathbf{r}(t_i)-\mathbf{r}(t_{i+1})}{t_i - t_{i+1}}. \tag{4.8}$$

These are the relevant quantities to investigate the scaling of the filament velocity and to asses the coherence of plasma filaments along a field line with varying curvature which is done in the following sections. The curvature is obtained for a single field line and assumed to be constant over the entire perpendicular domain.

4.4 Scalings

In section 3.5 different regimes for filament propagation are derived. In this section these are reproduced by numerical simulations of the `hermes-2` model. If parallel effects are discarded the charge separation is countered by the polarization current only. It has contributions from the time derivative of the perpendicular potential and ion pressure perturbation. If the former term dominates the filament velocity is expected to scale as $\delta_\perp^{1/2}$. For the latter term being larger, this leads to a $v_b \sim \delta_\perp^2$ scaling.
The parameters in these simulations are chosen as $T = 10\,\mathrm{eV}$, $N = 10^{18}\mathrm{m}^{-3}$. These are aligned with the parameters found in [44][58]. A scan with `hermes-2` simulations of the perpendicular blob size from 0ρ to 60ρ is displayed in figure 4.2. The amplitude of the density and temperature perturbation is 100% compared to the respective backgrounds. It is performed with three different electron-ion temperature ratios of $\tau_i = 0.025, 1$ and 3. The parallel current $j_\parallel$ is set to zero in the model equations.

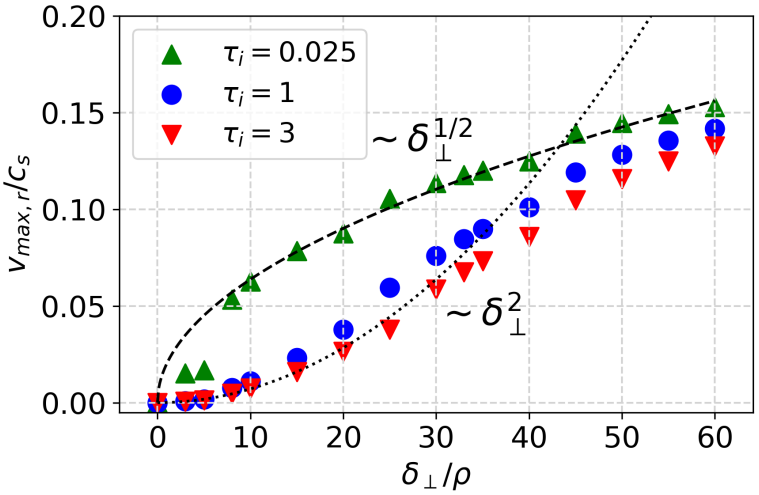

Figure 4.2: Inertial filament scalings without parallel current contributions. Small blobs propagate with a $\delta_\perp^2$ scaling, larger blobs change to a $\delta_\perp^{1/2}$ dependency. For larger τ_i the range of the $\delta_\perp^2$ scaling gets broader.

In order to keep the temperature ratios the energy exchange between electron and ion backgrounds W_i is switched off. The cold ion case ($\tau_i = 0.025$) only shows a $\delta_\perp^2$ scaling for very small filaments. For $\delta_\perp > 8\rho$ it follows a $\delta_\perp^{1/2}$ scaling which corresponds to the classical cold ion inertial scaling. Hot ion simulations show a $\delta_\perp^2$ dependence for much lager blobs up to $\delta_\perp \sim 40\rho$ before transitioning to the inertial regime. A larger τ_i leads to an increased p_i contribution in the vorticity which results in a larger term scaling as δ^2 in equation 3.10
If parallel currents are present, the dipole potential can also dissolved via the sheath which leads to a $\delta_\perp^{-2}$ scaling. This is the dominant mechanism for large blob sizes and small parallel connection lengths. Figure 4.3a shows $v_b/\delta_\perp$ scalings for cold ions ($\tau_i = 0.025$) at different connection lengths from 5 m to 100 m. The small τ_i leads

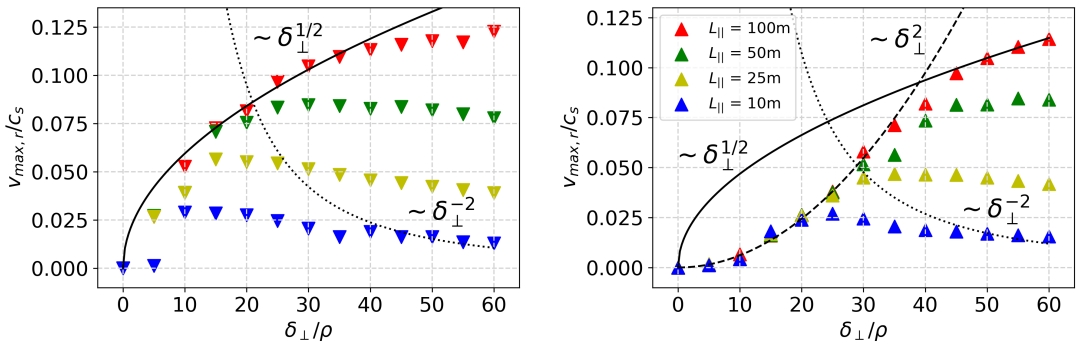

(a) (b)

Figure 4.3: Velocity scalings for cold ions (left, $\tau_i = 0.025$) and hot ions (right, $\tau_i = 3$) including sheath effects. The smallest blobs propagate in the $\delta_\perp^2$ scaling. Larger blobs follow the inertial scaling. The largest blobs propagate in the sheath limited regime scaling as $\delta_\perp^{-2}$. The sheath scaling δ^{-2} is only visible for the shortest connection lengths.

to the inertial term dominating the potential evolution. The 100 m case is barely influenced by the sheath and follows mostly the inertial regime while simulations for shorter connection lengths transition to the sheath limited regime. The shorter the connection length the smaller is the blob size at which the sheath effects dominate. The δ^2 regime is not present.
For hot ion simulations all three scalings discussed in section 3.5 are present. All simulations are ion pressure dominated for $\delta_\perp < 20\rho$ before inertial or sheath effects become significant depending on the connection length. With increasing $\delta_\perp$ filaments transition from the ion-inertial regime to the inertial and sheath limited regime. This is the case for the 10 m and 25 m cases. Longer $L_\parallel$ only show the inertial regimes.
These simulations highlight the basic dynamics of filament motion assuming parallel homogeneity. It has been shown that the `hermes-2` model in the applied setup can reproduce the analytical scalings as limit cases. This confirms that the relevant physical effects are included in the model. More complex effects can be studied. The next chapter introduces a varying curvature and studies the parallel effects which alter the motion of a filament and its coherence along the field line.

Chapter 5

Parallel Coherence of Filaments

This chapter presents simulations investigating the parallel coherence of blobs along a field line. Differential $\mathbf{E} \times \mathbf{B}$ drifts rip the filament apart if the parallel current does not even out the parallel potential gradient fast enough. The two main mechanisms limiting the parallel current in flattening the varying perpendicular charge separation are Ohmic resistance and electromagnetic inductance. Their effects on parallel coherence are discussed separate from each other in section 5.1 . Section 5.2 shows simulations combining both effects while the last section 5.3 of this chapter investigates the influence of a curvature variation on the averaged filament velocity.

5.1 Parametric Dependence of Filament Coherence

The simulations in the following three sections feature a sinusoidal curvature pointing in the radial x-direction. The $(\mathbf{b} \times \kappa)$ vector only has a z-component. The amplitude is approximately $1/R_{maj}$ with $R_{maj} = 1.65\,\mathrm{m}$ the major radius of AUG. The full z-component reads

$$(\mathbf{b} \times \kappa)_z = 0.6 \sin(y). \tag{5.1}$$

A filament of size $40\,\rho$ with $\tau_i = 3$ and the same properties as in section 4.4 is used for the simulations. Following the scaling in figure 4.3b this blob is mostly sheath dominated for an unperturbed curvature. The varying curvature leads to differing propagation speeds at different parallel positions. The difference in perpendicular displacement Δ is chosen as a measure for the parallel coherence of the structure. For the sinusoidal curvature profile used in the following sections Δ is determined by the difference between the position of the filament at the toroidal position of least curvature (y_{min}) and the position at the position of highest curvature (y_{max}) after one characteristic blob propagation time $\tau_b = \delta_\perp / v_b$

$$\Delta = \sqrt{(x(\tau_b, y_{min}) - x(\tau_b, y_{max}))^2 + (z(\tau_b, y_{min}) - z(\tau_b, y_{max}))^2}. \tag{5.2}$$

A filament is considered coherent for $\Delta/\delta_\perp < 1$ i.e. if the displacement after one blob propagation time τ_b is smaller than the initial blob of width $\delta_\perp$ The filament velocity v_b is determined by the potential, see equation 3.5. The dependence of Δ of the plasma control parameters ν and β_e is obtained from parallel Ohm's law.

Equation 3.27 can be rearranged for the parallel potential gradient

$$\partial_\parallel \phi = \frac{1}{2}\beta_e \partial_t \psi + \frac{1}{n}\partial_\parallel p_e + 0.71 \partial_\parallel T_e - \frac{\nu j_\parallel}{n} \tag{5.3}$$

which is connected to the parallel variation of the perpendicular velocity via $\partial_\parallel \phi = B\delta_\perp \partial_\parallel v_b$. The above equation can be integrated in time and rewritten with characteristic blob quantities to obtain a scaling for Δ. In the parallel direction quantities and parallel derivatives ($\partial_\parallel$) are expected to vary on the scale of the curvature variation L_κ. In the case of the sinusoidal curvature this is the distance between the minimum and maximum of the sine wave ($L_\kappa = L_\parallel/2$). The relevant time scale is the blob coherence time $\tau_b = \delta_\perp / v_b$. It is determined via a simulation with a constant curvature of 0.6 m. The average blob velocity is estimated to be one half of the maximum velocity the filament reaches in the unperturbed situation. Hence, the blob coherence time is approximated as $\tau_b \approx \delta_\perp / 2 v_{b,max}$. Stationary Ampere's law is employed to substitute the vector potential $j_\parallel = -\nabla_\perp^2 \psi \sim -\delta_\perp^{-2}\psi$. Integrating equation 5.3 gives an expression for the parallel displacement

$$\int_0^{\tau_b} \mathrm{d}t\, \partial_\parallel \phi \sim \delta_\perp \int_0^{\tau_b} \mathrm{d}t\, \partial_\parallel v_b \sim \frac{\left(v_b(y_{min}) - v_b(y_{max})\right)\tau_b \delta_\perp}{L_\kappa} := \frac{\Delta \delta_\perp}{L_\kappa}, \tag{5.4}$$

$$\Delta/\delta_\perp \sim -\left(\frac{\beta_e L_\kappa}{2} + \frac{\nu L_\kappa \tau_b}{n\delta_\perp^2}\right) j_\parallel + \frac{\tau_b}{n\delta_\perp^2} p_e + 0.71 \frac{\tau_b}{\delta_\perp^2} T_e. \tag{5.5}$$

Discarding the parallel pressure and temperature gradients gives a scaling law for the parallel coherence of a turbulent structure with control parameters ν and β_e. The neglected terms act against the Ohmic and inductive resistance terms. A similar calculation for parallel displacement has been performed for cold ion simulations considering parallel resistive drift wave instabilities [56]. A parallel varying curvature leads to an inhomogeneous filament drive due to varying divergence of the diamagnetic current. The response of the parallel current depends on the Ohmic and inductive resistance parallel to the magnetic field.

Figure 5.1 shows the parallel displacement of a filament with a sinusoidal curvature profile along the field line. The displacement follows the curvature. In this case ($n = 10^{19}\,\mathrm{m}^{-3}$, $T = 100\,\mathrm{eV}$) the parallel Ohmic and inductive resistance is large enough to hinder the parallel current sufficiently. The filament propagates in different directions at the position of minimal and maximal curvature.

The effects of Ohmic and inductive resistance are first illustrated separately. From the calculations in equation 5.4 the displacement between the minimum and the maximum of curvature is expected to scale as

$$\Delta/\delta_\perp \sim \left(\frac{\beta_e L_\kappa}{2} + \frac{\nu L_\kappa \tau_b}{n\delta_\perp^2}\right) j_\parallel := (\beta' + \nu')\, j_\parallel. \tag{5.6}$$

A larger normalized electron plasma beta β_e' or a larger normalized collisionality ν' increase the normalized parallel displacement $\Delta/\delta_\perp$.

For electrostatic simulations ($\beta_e = 0$) parallel current is only limited by the collisionallity ν. At constant temperature $T = 10\,\mathrm{eV}$ simulations with varying densities from $10^{18}\,\mathrm{m}^{-3}$ to $10^{19}\,\mathrm{m}^{-3}$ and $L_\parallel$ from 10 m to 200 m are computed. These are visible in figure 5.2a. The displacement first increases for higher normalized collisionality. The increase of the displacement for larger collisionalities disappears as the blob

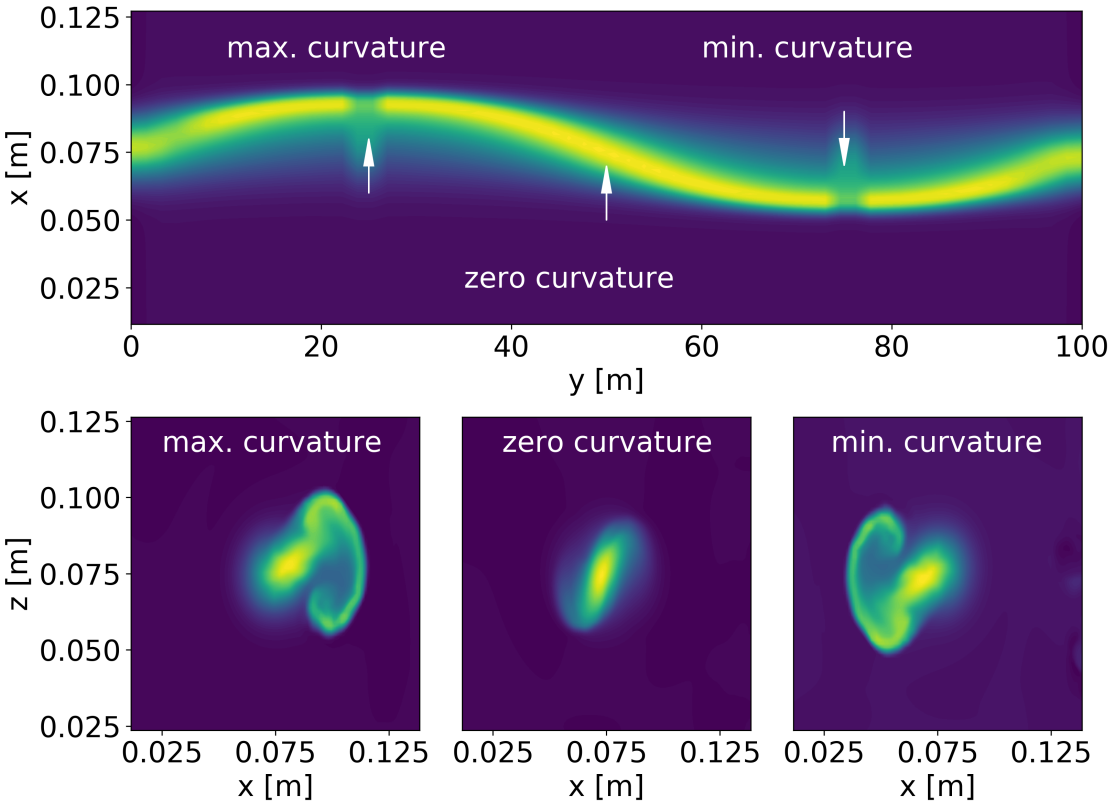

Figure 5.1: Perpendicular displacement of a filament as a result of inhomogeneous curvature drive along the magnetic field line. Here, a high β_e' dampens the parallel current. The differential $\mathbf{E} \times \mathbf{B}$ advection shears the filament apart. The part subject to a negative drive propagates backwards. The filament in the region of maximum curvature propagates radially outwards. In the middle where the drive vanishes structures that propagate parallel due to the flattening of the pressure gradient appear.

dynamics is fully determined by perpendicular effects and parallel currents do not have a significant influence anymore.

A similar picture appears for simulations with high β_e' and low ν' in figure 5.2b. Here, the temperature is 100 eV. The densities and parallel connection lengths are kept the same. The parallel current is primarily limited by the inductance. At sufficiently high β_e' the parallel current is entirely damped on the advection timescale. This is the timescale in which a blob travels a distance of $\delta_\perp$. A further increase in β_e' does not influence the perpendicular blob dynamics.

The above equation 5.6 discards the pressure term in parallel Ohm's law 3.27. A parallel pressure gradient drives a parallel flow. The influence of the $\partial_\parallel p_e$ contribution is larger compared to the collisionality and electromagnetic terms for lower connection lengths as both expressions of β_e' and ν' scale linearly with $L_\parallel$ and $\partial_\parallel p_e$ scales as $p_e/L_\parallel$. Simulations with similar normalized collisionality ν' or β_e' show higher displacement for longer $L_\parallel$. This explains the scattering of the displacement values in figures 5.2a and 5.2b.

The different saturation levels in figures 5.2a and 5.2b can be understood from the velocity scalings. The temperature is 10 eV in the collisionally dominated regime and 100 eV in the electromagnetically dominated regime. The blob used in these

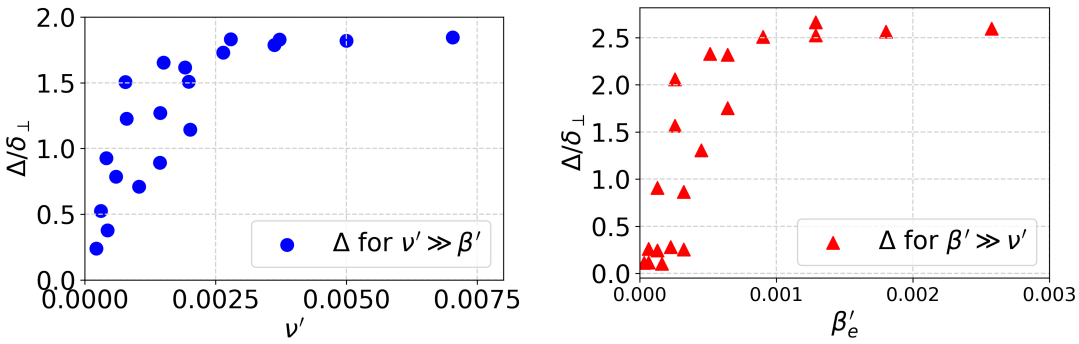

(a) (b)

Figure 5.2: Normalized displacement of filaments subject to a sinusoidal curvature for collisionally (left) and electromagnetically (right) dominated regimes. The displacement increases as the parallel current is limited by Ohmic resistance or inductance thus disconnecting parallel separate regions. For large β'_e or ν', the parallel current does not have any influence on the advection timescale. The displacement does not further increase. Different saturation levels are due to the different absolute blob sizes. The blob size is kept at 40ρ, the Larmor radius changes.

simulations has an initial size of $40\,\rho$. Due to the high collisionality or electron plasma beta, the blob propagates in the inertial regime, so $v_b \sim \delta^{1/2}$. The Larmor radius scales with the square root of the temperature, therefore $v_b \sim (40\rho)^{1/2} \sim T^{1/4}$ and the ratio between the displacements which scale with the velocity according to equation 5.4 is expected to be equal. Indeed, the ratio of the two blob velocities is $10^{1/4} \approx 1.7$. The ratio of the saturation displacements is approximately 1.4 and lies in a similar range.

5.2 Multidimensional Parameter Dependence of Filament Coherence

The influence of the two main control parameters β'_e and ν' has been examined separately in the previous section. Both effects can be combined to cover the parameter space relevant for filamentary transport in toroidal fusion devices. The parameter scan behind figure 5.3 covers densities from $10^{18}\,\mathrm{m}^{-3}$ to $10^{19}\,\mathrm{m}^{-3}$, temperatures from 10 eV to 100 eV and parallel connection lengths from 25 m to 200 m. This leads to a two dimensional evaluation of the parallel coherence of turbulent structures for a relevant (β'_e, ν') space. The displacement between the maximum and minimum of the normal curvature increases from the bottom left to the top right. High (β'_e, ν') lead to significant displacements larger than the initial blob size $\delta_\perp$. The parallel current is not able to resolve the parallel potential gradient $\partial_\parallel \phi$ fast enough.
The simulations can be classified in two ways: They differ in their coherence. Incoherent blobs reach $\Delta > \delta_\perp$. For coherent filaments the normalized displacement stays below unity. The other distinction is between the dominant limiting factor for the parallel current. It is either bound by collisional or electromagnetic effects. In figure 5.3 these different regimes are indicated by a $(\nu' = \beta'_e)$ line and two lines perpendicular to the former indicating $\Delta < \delta_\perp$ and $\Delta > \delta_\perp$. The influence of the

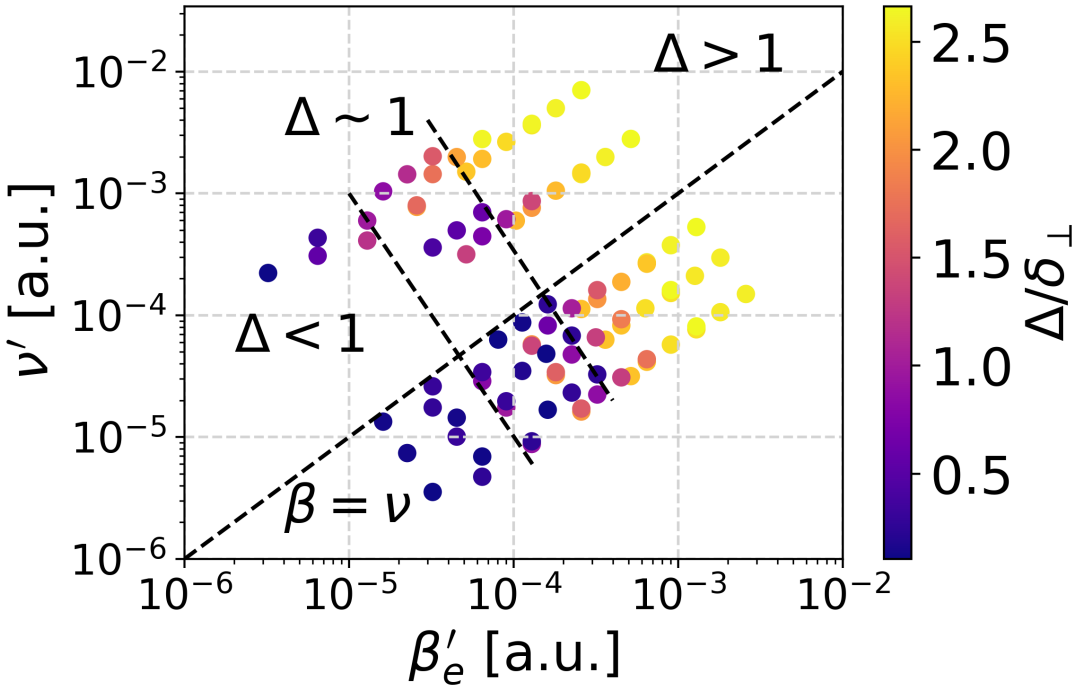

Figure 5.3: Normalized displacement of filaments for a sinusoidal curvature drive in (β_e', ν') space for temperatures from 10 eV to 100 eV and densities from $10^{18}\,\mathrm{m}^{-3}$ to $10^{19}\,\mathrm{m}^{-3}$. The displacement is largest for large $\beta_e' + \nu'$.

pressure term described in section 5.1 leads to simulations where very similar (β_e', ν') show different displacements depending on the parallel connection length. Higher $L_\parallel$ cause higher displacements as the pressure gradient $\partial_\parallel p_e$ drives a parallel flow which acts against the Ohmic and inductive terms and scales as $1/L_\parallel$

5.3 Influence of Varying Curvature on Filament Velocity

The local curvature in this section can be considered to be the sum of the average curvature $\bar{\xi}$ and a sinusoidal variation with amplitude $\tilde{\xi}$ so that $\xi = \bar{\xi} + \tilde{\xi}\sin(y)$. Figure 5.4 shows the maximum averaged velocity of a filament of size $\delta_\perp = 30\,\rho$ against the relative curvature variation $\tilde{\xi}/\bar{\xi}$. In the following simulations $\bar{\xi} = 0.6\,\mathrm{m}^{-1}$ is chosen. The small increase in velocity for $\tilde{\xi}/\bar{\xi} < 1$ compared to the simulation with no variation can be attributed to the influence of the sheath boundary condition on the COM calculation. It influences parts of the blob farther away from the boundary at $y = 0$ and $y = L_\parallel$ for the 10 eV cases.
For $\tilde{\xi}/\bar{\xi} > 1$ the curvature variation leads to a significant deceleration of the filament compared to the unperturbed case. This effect is increased for larger contributions of inductance and resistance (β_e', ν'). In Figure 5.4 the effect of the varying curvature is much stronger for $n = 10^{19}\,\mathrm{m}^{-3}$, $T = 100\,\mathrm{eV}$ compared to $n = 10^{18}\,\mathrm{m}^{-3}$, $T = 10\,\mathrm{eV}$. In the most extreme case, the velocity is less than half compared to the unperturbed case.

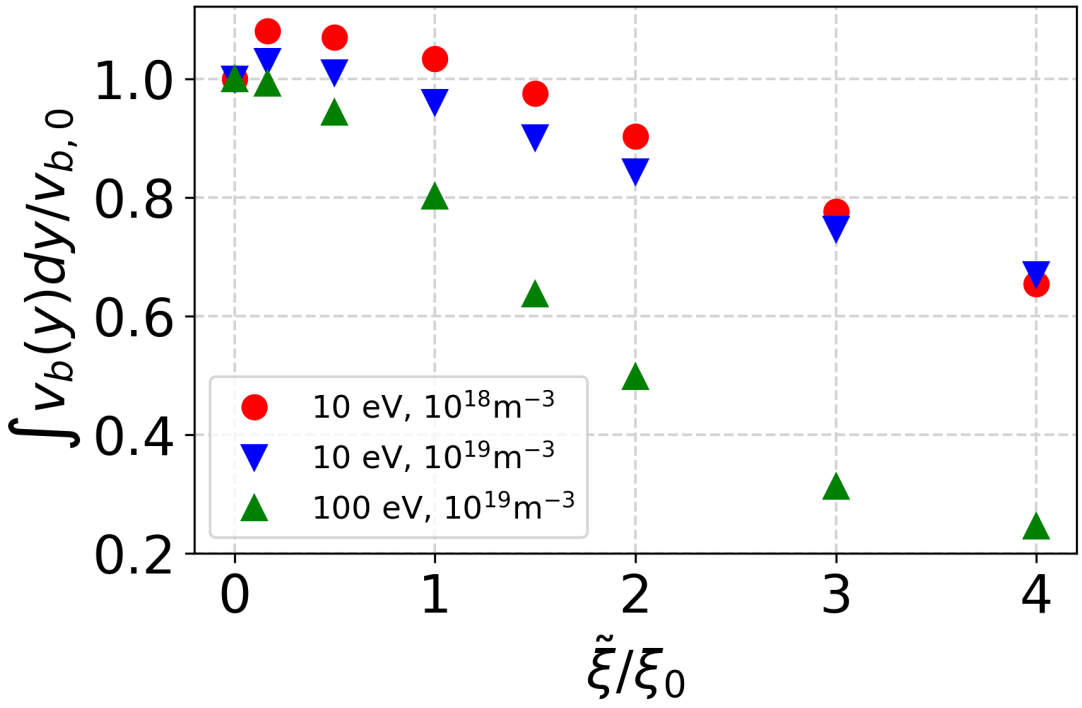

Figure 5.4: Toroidally averaged velocities for filaments with an average curvature drive plus a sinusoidal perturbation. For large perturbation amplitudes the averaged filament velocity decreases significantly for higher β_e' or ν'.

The deceleration of the filament is caused by parallel flows driven by $\partial_\parallel p_e$ decrease the amplitude of the perpendicular pressure perturbation and therefore the filament drive. For $\tilde{\xi} \geq \bar{\xi}$ this contribution of the varying curvature to the filament velocity becomes dominant over the average curvature drive leading to significant displacements. The filament loses parallel coherence.
In the following chapter realistic magnetic geometries in tokamaks and stellarators are simulated. The insights gained in this chapter are used to evaluate the coherence of filaments for these cases.

Chapter 6

Simulations of realistic field lines

In this chapter the insights about filament coherence from the previous chapter 5 are applied to realistic cases. Two cases are investigated: the curvature of a circular tokamak which has been derived in section 3.6 and the curvature of a field line in W-7X. The latter field line crosses the field of view of a newly installed Gas Puff Imaging diagnostic (GPI) that will be used in the next operation phase.

6.1 Circular Tokamak

In this section simulations with the curvature profile of a circular tokamak calculated in section 3.6 are performed. The expressions for geodesic and normal curvature read

$$\kappa_n = -\frac{1}{1+\left(\frac{r}{qR_0}\right)^2}\left(\frac{r}{q^2R_0^2}+\frac{\cos(\theta)}{R_0+r\cos(\theta)}\right) \text{ and} \tag{6.1}$$

$$\kappa_g = \frac{1}{\sqrt{1+\left(\frac{r}{qR_0}\right)^2}}\frac{\sin(\theta)}{R_0+r\cos(\theta)}.$$

With AUG-like parameters ($R_0 = 1.6\,\mathrm{m}$, $r = 0.5\,\mathrm{m}$, $q = 4$) the blob temperatures and densities are taken from measurements in AUG L-Mode plasmas [44]. The simulation domain has the dimensions $L_\perp = 0.15\,\mathrm{m}$ and $L_\parallel = 100\,\mathrm{m}$. The resolution is $132 \times 64 \times 128$.

Figure 6.1 shows the displacement in radial and binormal direction. The radial displacement correlates with the binormal component of the vector $(\mathbf{b}\times\kappa)_z \approx -\kappa_n$. The radial component of this vector is similar to the geodesic curvature and correlates with the binormal displacement. The local curvature drives the charge separation which leads to differential $\mathbf{E}\times\mathbf{B}$ advection. The difference in displacement is increased for a higher ion temperature as this increases the curvature drive. For AUG-like parameters the displacement stays smaller than the perpendicular blob size. The parallel current resolves the potential too fast to create significant displacement. This can be understood from the displacement scaling from the previous section.

$$\Delta/\delta_\perp \sim \left(\frac{\beta_e L_\kappa}{2}+\frac{\nu L_\kappa \tau_b}{n\delta_\perp^2}\right) j_\parallel := (\beta'+\nu')\, j_\parallel. \tag{6.2}$$

The AUG-like parameters ($10\,\mathrm{eV}$, $10^{18}\,\mathrm{m}^{-3}$) correspond to the lower end of the (β_e', ν') parameter space spanned in figure 5.3. The densities and temperatures in

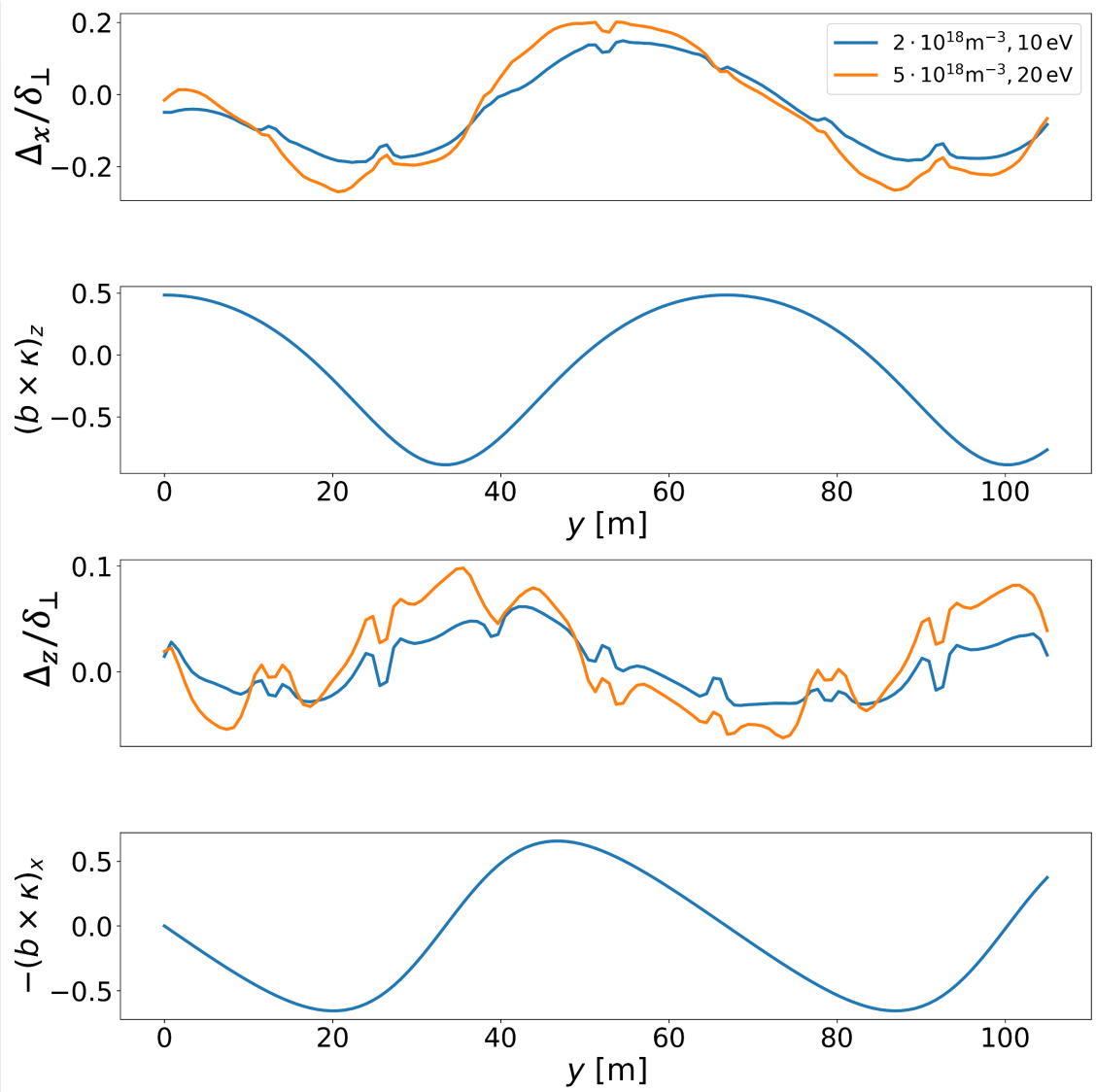

Figure 6.1: Radial and binormal displacement of a filament in a circular tokamak with AUG-like parameters. The displacement correlates with the respective components of the $\mathbf{b} \times \kappa$ vector which drives the charge separation.

this plot range from $10^{18}\,\mathrm{m}^{-3}$ $10^{19}\,\mathrm{m}^{-3}$ and from to 10 eV to 100 eV, respectively. The temperature and density are comparatively low while the curvature fall-off length is similar to the sinusoidal curvature used during section 5.1 with $L_\parallel = 100\,\mathrm{m}$. The displacement of the equivalent datapoint in figure 5.3 is $\Delta/\delta_\perp = 0.79$. This is higher than the displacement observed in this simulation ($\Delta/\delta_\perp = 0.34$), which can be explained by the lower density and pressure perturbations compared to the previous section. The low displacement observed for AUG-like parameters in a circular tokamak is compatible with the parameter dependences found for sinusoidal curvature. For higher density and temperature ($5 \cdot 10^{18}\,\mathrm{m}^{-3}$, 50 eV) a higher normalized displacement of 0.47 is found, which compares similarly to the analogous displacement from figure 5.3 of 1.27.

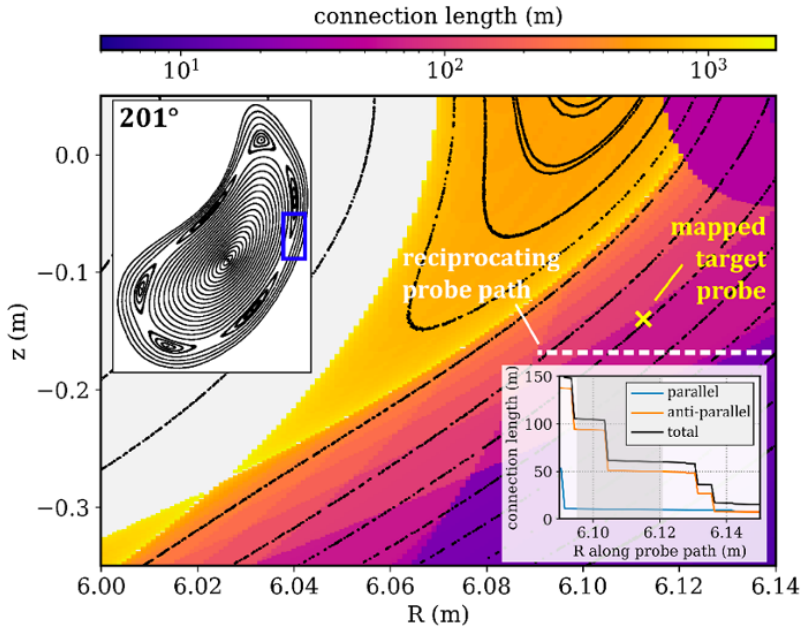

Figure 6.2: The W7-X scrape-off layer. The stellarator magnetic field and the magnetic island chain around the primary separatrix lead to a highly varying parallel connection length and curvature [66].

6.2 W7-X Field Line

In the next Operation Phase of W7-X there will be a Gas Puff Imaging diagnostic installed to investigate the plasma edge near a magnetic island [79]. This region experiences a strong variation in the parallel connection length as well as a highly inhomogeneous curvature. Effects of a transition in $L_\parallel$ have been investigated in [80]. The following simulations are similar to the simulations with sinusoidal curvature from the previous chapter but feature the realistic curvature profile of a W7-X field line crossing the line of sight of this diagnostic.
Simulations are performed in which a filament is initialized as a Gaussian pressure perturbation homogeneous along a field line. The curvature profile of the W7-X field line taken from the IPP-Webservices [54]. The curvature is calculated using a field line tracer provided by Dr. Carsten Killer. The information about blob size and density are taken from recent experimental studies [66]. The filament is initialized with $\delta_\perp \approx 1\,\mathrm{cm}$, a background density of $6 \cdot 10^{18}\,\mathrm{m}^{-3}$ and a density perturbation of 30% above the background. The electron and normalization temperature is 22 eV with a 10% perturbation. There is no measurement of ion background temperature and fluctuations in W7-X. Therefore, three different cases are investigated: a cold ion case with $\tau_i = 0.1$, a case with equal electron and ion temperature ($\tau_i = 1$) and a hot ion case ($\tau_i = 3$). The relative ion temperature fluctuation amplitude is set to 10%. The perpendicular displacement along the field line correlates with the curvature which can be seen in figure 6.4. This is similar to the simulations of circular tokamak curvature in the previous section. The simulations with $\tau_i = 0.025$ and 1 show a very small displacement. For the hot ion case the displacement at the most prominent curvature feature exceed one blob size. The displacement is increased for higher τ_i as this increases the overall pressure perturbation and the curvature drive. The displacement of the most similar datapoint ($5 \cdot 10^{18}, 20\,\mathrm{eV}$) with sinusoidal cur-

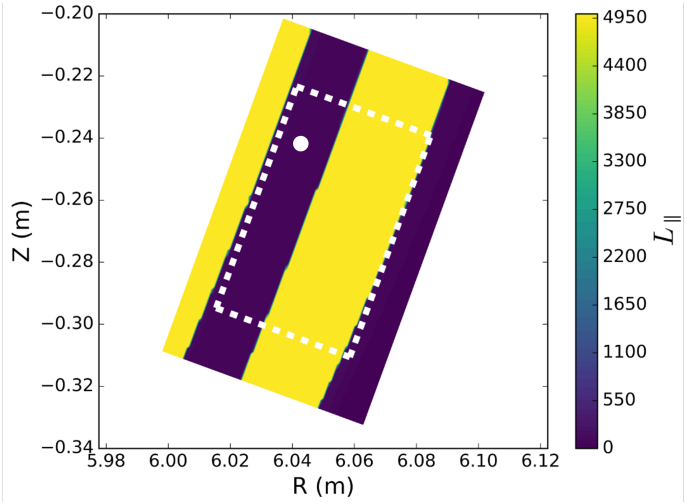

Figure 6.3: The field of view of the GPI diagnostic with the $L_\parallel$ profile [67]. The white dot indicates the position where the field line used in this section crosses the plane of sight. The island divertor creates regions of closed field lines (yellow) outwards of the primary separatrix.

vature is $\Delta/\delta_\perp = 2.12$. This is much higher compared to the W7-X simulations with $\tau_i = 3$. This can be once again understood from the scaling as explained in the following.

The displacement in formula 5.6 scales linearly with the curvature fall off length which is much shorter for the W7-X field line compared to the sinusoidal case in the previous chapter 5. It shows thin localized spikes of curvature. As the parallel connection length is 105 m the curvature fall of length is approximately 10 m. The simulations in chapter 5 are performed on a sinusoidal curvature with only one period along the field line. The curvature fall off length is $L_\parallel/2 = 50\,\mathrm{m}$. Additionally, the density and temperature perturbations are smaller. The density perturbation is only 30% compared to 100% in chapters 4 and 5. The drive of the filaments is reduced compared to the previous simulations.

The simulations with $\tau_i = 0.025$ and 1 show almost no filament propagation despite an average normal curvature of about $0.016\,\mathrm{m}^{-1}$. The weak curvature is not able to drive significant $\mathbf{E} \times \mathbf{B}$ advection. The high variation reduces the propagation further compared to a simulation with the average curvature of W7-X. This is consistent with the findings from the simulations with average drive and snd sinusoidal variation in section 5.3.

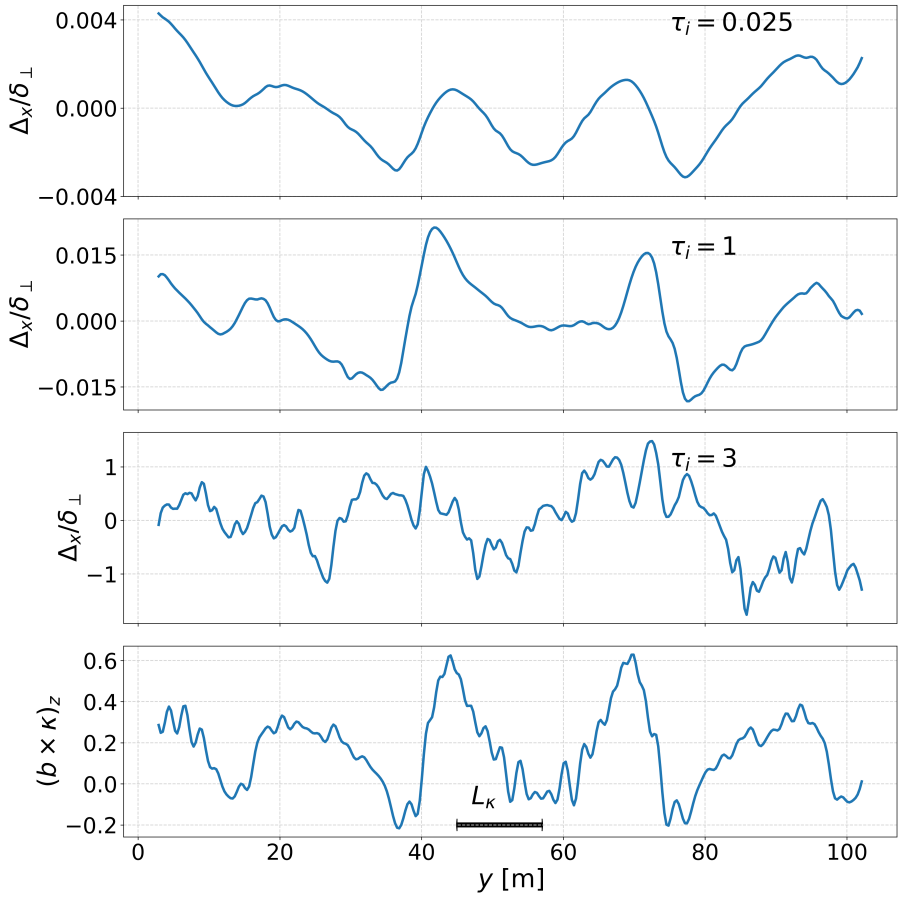

Figure 6.4: Radial displacement of a filament along a field line at the observation point of the new GPI diagnostic and the binormal component of the $\mathbf{b} \times \kappa$ vector. The curvature fall-off length L_κ of the most prominent curvature feature is indicated. The displacement follows the curvature. It increases with an increased amplitude of the ion pressure perturbation which increases the drive.

Chapter 7

Summary

In this thesis the `hermes-2` model equations are solved by means of the `BOUT++` framework to investigate the coherence of filaments experiencing a parallel varying curvature drive.
The different scalings of the filament velocity with the perpendicular blob size $\delta_\perp$ are reproduced in simulations with constant curvature to show that `hermes-2` contains the important physical effects to describe filament physics:
If the potential dipole of the filament is primarily reduced by the ion pressure term ($\sim \Delta_\perp p_i$) of the polarization current, the velocity scales as $v_b \sim \delta_\perp^2$. For the inertial term ($\sim \Delta_\perp \phi$) dominating the polarization current, the scaling is $\sim \delta_\perp^{1/2}$. In figure 4.2 it is visible that the $\delta_\perp^2$ scaling is found for smaller filaments. This scaling disappears for the cold ion case, which only shows a $\delta_\perp^{1/2}$ velocity dependence.
If the parallel current dominates the current balance the velocity scales as $\delta_\perp^{-2}$. Figures 4.3a and 4.3b show the filament velocity for parallel connection lengths from 10 m to 100 m for cold and hot ions respectively. The δ^2 scaling arises for high perpendicular filament sizes and low parallel connection lengths. Filaments in these simulations at a density of $10^{18}\,\mathrm{m}^{-3}$ and temperatures between 10 eV and 100 eV with a constant curvature of $0.6\,\mathrm{m}^{-1}$ propagate with speeds of up to 12% of the sound speed.
For a constant curvature the filament is evenly elongated along the magnetic field line. A parallel varying curvature leads to a varying charge separation causing differential $\mathbf{E} \times \mathbf{B}$ advection along the field line. The parallel current sets in to reduce the inhomogeneous polarization. If the parallel current flattens the parallel potential gradient fast enough, the filament stays coherent along the field line. Otherwise, the differential $\mathbf{E} \times \mathbf{B}$ advection rips the filament apart into separate structures. The parallel displacement between the point of lowest and the point of highest curvature is chosen as a measure of filament coherence. The displacement Δ is normalized to the perpendicular blob size $\delta_\perp$. A filament is considered coherent for $\Delta/\delta_\perp < 1$.
The evolution of the parallel current is governed by parallel Ohm's law with the main control parameters being collisionallity ν and the electron plasma beta β_e governing the Ohmic resistance and the inductance terms. Normalized via the blob correspondence principle ν' and β_e' control the propagation time of the parallel current and determine the parallel displacement of different parts of the filament. High ν' and β_e' increase the propagation of the parallel current $j_\parallel$ against the perpendicular advection time of the blob allowing for differential displacement.
Simulations for $\beta_e' \to 0$ and $\nu' \to 0$ are shown in figures 5.2a and 5.2b, where

the normalized displacement $\Delta/\delta_\perp$ is governed by only ν' or β'_e, respectively. The maximum displacement is found to be $\Delta/\delta_\perp = 2.67$. These results are compatible with previous work on the coherence of filaments [68]. There, an increase in temperature has been found to increase filament coherence. As these simulations were electrostatic ($\beta_e = 0$) an increase in temperature decreases the collisionality which decreases the parallel displacement.
The combined influence of ν' and β'_e is displayed in figure 5.3. Simulations with a sinusoidal curvature variation along the field line show significant displacement for sufficiently high values of $(\nu' + \beta'_e)$, exceeding the perpendicular blob size $\delta_\perp$. Deviations from the scaling $\Delta/\delta_\perp \sim (\nu' + \beta'_e)j_\parallel$ arise from the influence of the parallel pressure gradient $\partial_\parallel p_e \sim 1/L_\parallel p_e$. Its influence is increased for smaller connection lengths and it acts against the Ohmic and inductive resistance terms. Therefore, simulations with similar values of $(\nu' + \beta'_e)$ show larger displacements for higher parallel connection lengths.
A sinusoidal curvature with an additional constant curvature drive is shown to decrease the filament velocity compared to the homogeneous curvature case if the amplitude of the variation is of similar magnitude as the average drive. This is shown in figure 5.4. A large displacement leads to parallel flows driven by parallel pressure gradients $\partial_\parallel p_e$. This decreases the amplitude of the perpendicular pressure perturbation reducing the drive of filament motion. For a density of $10^{19}\mathrm{m}^{-3}$ and a temperature of 100 eV which corresponds to comparatively high $(\nu' + \beta'_e)$ in figure 5.3 the filament velocity is reduced to $\approx 40\%$ of the unperturbed case for a curvature variation four times higher than the average curvature.
Simulations of filaments in a circular tokamak and simulations of a field line from W7-X in areas relevant for a future diagnostic show displacements compatible to the previously motivated parameter dependences. The displacement along the field line follows the curvature profile in the radial and binormal direction. Simulations with blob and background temperature and density inputs from AUG measurements in figure 6.1 show a small radial displacement of 0.34. This is compatible to the results from figure 5.3 as the pressure perturbations in the tokamak simulations are smaller. The W7-X-like curvature shows thin localized spikes of high curvature. This results in the normalized displacement exceeding one perpendicular blob size at the most prominent curvature feature. This is displayed in figure 6.4 and fits the displacement scaling as the curvature fall-off length and the pressure perturbations are lower.
The strong variation decreases the filament velocity to almost zero. This is in agreement with recent experimental findings [66] which show that filaments in W7-X are approximately bound to their initial flux surface and do not perform ballistic motion or turbulence spreading in the scrape-off layer.
The hot-ion `hermes-2` code used in this thesis provides a flexible tool to simulate filament and turbulent dynamics. Filaments can be investigated for their velocity, coherence and secondary instabilities. It is viable for different positions in the SOL. This can be applied to other W7-X or tokamak configurations in the future. In particular, `hermes-2` is planned to investigate the temperature dynamics of filaments during their propagation through the SOL. This project will center on the role of the collisional energy exchange between energy and ions.

Bibliography

[1] H. Ritchie and M. Roser, "Energy," *Our world in data*, 2020. [Online]. Available: https://ourworldindata.org/energy

[2] O. Jarvis, "Kaye and laby: 4.7.4 nuclear fusion," 2018. [Online]. Available: https://web.archive.org/web/20181208184556/http://www.kayelaby.npl.co.uk/atomic_and_nuclear_physics/4_7/4_7_4.html

[3] N. N. D. Center, "information extracted from the nudat 2 database." [Online]. Available: https://www.nndc.bnl.gov/nudat2/

[4] Umweltbundesamt, "Stromverbrauch." [Online]. Available: https://www.umweltbundesamt.de/daten/energie/stromverbrauch

[5] J. Lawson, "Some criteria for a power producing thermonuclear reactor," 1957, pp. 6–10.

[6] M. Laberge, "Magnetized target fusion with a spherical tokamak," *Journal of Fusion Energy*, vol. 38, pp. 199–203, 2 2019.

[7] M. L. Spaeth, K. R. Manes, D. H. Kalantar, P. E. Miller, J. E. Heebner, E. S. Bliss, D. R. Spec, T. G. Parham, P. K. Whitman, P. J. Wegner, P. A. Baisden, J. A. Menapace, M. W. Bowers, S. J. Cohen, T. I. Suratwala, J. M. D. Nicola, M. A. Newton, J. J. Adams, J. B. Trenholme, R. G. Finucane, R. E. Bonanno, D. C. Rardin, P. A. Arnold, S. N. Dixit, G. V. Erbert, A. C. Erlandson, J. E. Fair, E. Feigenbaum, W. H. Gourdin, R. A. Hawley, J. Honig, R. K. House, K. S. Jancaitis, K. N. LaFortune, D. W. Larson, B. J. L. Galloudec, J. D. Lindl, B. J. MacGowan, C. D. Marshall, K. P. McCandless, R. W. McCracken, R. C. Montesanti, E. I. Moses, M. C. Nostrand, J. A. Pryatel, V. S. Roberts, S. B. Rodriguez, A. W. Rowe, R. A. Sacks, J. T. Salmon, M. J. Shaw, S. Sommer, C. J. Stolz, G. L. Tietbohl, C. C. Widmayer, and R. Zacharias, "Description of the nif laser," *Fusion Science and Technology*, vol. 69, 2 2016.

[8] C. C. Petty, R. Nazikian, J. M. Park, F. Turco, X. Chen, L. Cui, T. E. Evans, N. M. Ferraro, J. R. Ferron, A. M. Garofalo, B. A. Grierson, C. T. Holcomb, A. W. Hyatt, E. Kolemen, R. J. L. Haye, C. Lasnier, N. Logan, T. C. Luce, G. R. McKee, D. Orlov, T. H. Osborne, D. C. Pace, C. Paz-Soldan, T. W. Petrie, P. B. Snyder, W. M. Solomon, N. Z. Taylor, K. E. Thome, M. A. V. Zeeland, and Y. Zhu, "Advances in the steady-state hybrid regime in diii-d - a fully non-inductive, elm-suppressed scenario for iter," *Nuclear Fusion*, vol. 57, 8 2017.

[9] H. Zohm, "On the size of tokamak fusion power plants," vol. 377. Royal Society Publishing, 3 2019.

[10] M. Hirsch, J. Baldzuhn, C. Beidler, R. Brakel, R. Burhenn, A. Dinklage, H. Ehmler, M. Endler, V. Erckmann, Y. Feng, J. Geiger, L. Giannone, G. Grieger, P. Grigull, H. J. Hartfuß, D. Hartmann, R. Jaenicke, R. König, H. P. Laqua, H. Maaßberg, K. McCormick, F. Sardei, E. Speth, U. Stroth, F. Wagner, A. Weller, A. Werner, H. Wobig, and S. Zoletnik, "Major results from the stellarator wendelstein 7-as," *Plasma Physics and Controlled Fusion*, vol. 50, 2008.

[11] J. M. Canik, D. T. Anderson, F. S. B. Anderson, K. M. Likin, J. N. Talmadge, and K. Zhai, "Experimental demonstration of improved neoclassical transport with quasihelical symmetry," *Physical Review Letters*, vol. 98, p. 085002, 2 2007.

[12] R. Wolf, A. Ali, A. Alonso, J. Baldzuhn, C. Beidler, M. Beurskens, C. Biedermann, H.-S. Bosch, S. Bozhenkov, R. Brakel, A. Dinklage, Y. Feng, G. Fuchert, J. Geiger, O. Grulke, P. Helander, M. Hirsch, U. Höfel, M. Jakubowski, J. Knauer, G. Kocsis, R. König, P. Kornejew, A. Krämer-Flecken, M. Krychowiak, M. Landreman, A. Langenberg, H. Laqua, S. Lazerson, H. Maaßberg, S. Marsen, M. Marushchenko, D. Moseev, H. Niemann, N. Pablant, E. Pasch, K. Rahbarnia, G. Schlisio, T. Stange, T. S. Pedersen, J. Svensson, T. Szepesi, H. T. Mora, Y. Turkin, T. Wauters, G. Weir, U. Wenzel, T. Windisch, G. Wurden, D. Zhang, I. Abramovic, S. Äkäslompolo, P. Aleynikov, K. Aleynikova, R. Alzbutas, G. Anda, T. Andreeva, E. Ascasibar, J. Assmann, S.-G. Baek, M. Banduch, T. Barbui, M. Barlak, K. Baumann, W. Behr, A. Benndorf, O. Bertuch, W. Biel, D. Birus, B. Blackwell, E. Blanco, M. Blatzheim, T. Bluhm, D. Böckenhoff, P. Bolgert, M. Borchardt, V. Borsuk, J. Boscary, L.-G. Böttger, H. Brand, C. Brandt, T. Bräuer, H. Braune, S. Brezinsek, K.-J. Brunner, B. Brünner, R. Burhenn, B. Buttenschön, V. Bykov, I. Calvo, B. Cannas, A. Cappa, A. Carls, L. Carraro, B. Carvalho, F. Castejon, A. Charl, F. Chernyshev, M. Cianciosa, R. Citarella, Ciupiński, G. Claps, M. Cole, M. Cole, F. Cordella, G. Cseh, A. Czarnecka, A. Czermak, K. Czerski, M. Czerwinski, G. Czymek, A. da Molin, A. da Silva, G. Dammertz, A. de la Pena, S. Degenkolbe, P. Denner, D. Dhard, M. Dostal, M. Drevlak, P. Drewelow, P. Drews, A. Dudek, G. Dundulis, F. Durodie, P. van Eeten, F. Effenberg, G. Ehrke, M. Endler, D. Ennis, E. Erckmann, H. Esteban, T. Estrada, N. Fahrenkamp, J.-H. Feist, J. Fellinger, H. Fernandes, W. Fietz, W. Figacz, J. Fontdecaba, O. Ford, T. Fornal, H. Frerichs, A. Freund, M. Führer, T. Funaba, A. Galkowski, G. Gantenbein, Y. Gao, J. G. Regaña, M. Garcia-Munoz, D. Gates, G. Gawlik, B. Geiger, V. Giannella, N. Gierse, A. Gogoleva, B. Goncalves, A. Goriaev, D. Gradic, M. Grahl, J. Green, A. Grosman, H. Grote, M. Gruca, C. Guerard, L. Haiduk, X. Han, F. Harberts, J. Harris, H.-J. Hartfuß, D. Hartmann, D. Hathiramani, B. Hein, B. Heinemann, P. Heitzenroeder, S. Henneberg, C. Hennig, J. H. Sanchez, C. Hidalgo, H. Hölbe, K. Hollfeld, A. Hölting, D. Höschen, M. Houry, J. Howard, X. Huang, M. Huber, V. Huber, H. Hunger, K. Ida, T. Ilkei, S. Illy, B. Israeli, A. Ivanov, S. Jablonski, J. Jagielski, J. Jelonnek, H. Jenzsch, P. Junghans, J. Kacmarczyk, T. Kaliatka,

J.-P. Kallmeyer, U. Kamionka, R. Karalevicius, H. Kasahara, W. Kasparek, N. Kenmochi, M. Keunecke, A. Khilchenko, D. Kinna, R. Kleiber, T. Klinger, M. Knaup, T. Kobarg, F. Köchl, Y. Kolesnichenko, A. Könies, M. Köppen, J. Koshurinov, R. Koslowski, F. Köster, R. Koziol, M. Krämer, R. Krampitz, P. Kraszewsk, N. Krawczyk, T. Kremeyer, T. Krings, J. Krom, G. Krzesinski, I. Ksiazek, M. Kubkowska, G. Kühner, T. Kurki-Suonio, S. Kwak, R. Lang, S. Langish, H. Laqua, R. Laube, C. Lechte, M. Lennartz, W. Leonhardt, L. Lewerentz, Y. Liang, C. Linsmeier, S. Liu, J.-F. Lobsien, D. Loesser, J. L. Cisquella, J. Lore, A. Lorenz, M. Losert, L. Lubyako, A. Lücke, A. Lumsdaine, V. Lutsenko, J. Majano-Brown, O. Marchuk, M. Mardenfeld, P. Marek, S. Massidda, S. Masuzaki, D. Maurer, K. McCarthy, P. McNeely, A. Meier, D. Mellein, B. Mendelevitch, P. Mertens, D. Mikkelsen, O. Mishchenko, B. Missal, J. Mittelstaedt, T. Mizuuchi, A. Mollen, V. Moncada, T. Mönnich, T. Morizaki, R. Munk, S. Murakami, F. Musielok, G. Náfrádi, M. Nagel, D. Naujoks, H. Neilson, O. Neubauer, U. Neuner, T. Ngo, R. Nocentini, C. Nührenberg, J. Nührenberg, S. Obermayer, G. Offermanns, K. Ogawa, J. Ongena, J. Oosterbeek, G. Orozco, M. Otte, L. P. Rodriguez, W. Pan, N. Panadero, N. P. Alvarez, A. Panin, D. Papenfuß, S. Paqay, A. Pavone, E. Pawelec, G. Pelka, X. Peng, V. Perseo, B. Peterson, A. Pieper, D. Pilopp, S. Pingel, F. Pisano, B. Plaum, G. Plunk, M. Povilaitis, J. Preinhaelter, J. Proll, M.-E. Puiatti, A. P. Sitjes, F. Purps, M. Rack, S. Récsei, A. Reiman, D. Reiter, F. Remppel, S. Renard, R. Riedl, J. Riemann, S. Rimkevicius, K. Riße, A. Rodatos, H. Röhlinger, M. Romé, P. Rong, H.-J. Roscher, B. Roth, L. Rudischhauser, K. Rummel, T. Rummel, A. Runov, N. Rust, L. Ryc, S. Ryosuke, R. Sakamoto, A. Samartsev, M. Sanchez, F. Sano, S. Satake, G. Satheeswaran, J. Schacht, F. Schauer, T. Scherer, A. Schlaich, K.-H. Schlüter, J. Schmitt, H. Schmitz, O. Schmitz, S. Schmuck, M. Schneider, W. Schneider, M. Scholz, P. Scholz, R. Schrittwieser, M. Schröder, T. Schröder, R. Schroeder, H. Schumacher, B. Schweer, B. Shanahan, I. Shikhovtsev, M. Sibilia, P. Sinha, S. Sipliä, J. Skodzik, C. Slaby, H. Smith, W. Spiess, D. Spong, A. Spring, R. Stadler, B. Standley, L. Stephey, M. Stoneking, U. Stridde, Z. Sulek, Y. Suzuki, V. Szabó, T. Szabolics, Z. Szökefalvi-Nagy, N. Tamura, A. Terra, J. Terry, J. Thomas, H. Thomsen, M. Thumm, C. von Thun, D. Timmermann, P. Titus, K. Toi, J. Travere, P. Traverso, J. Tretter, H. Tsuchiya, T. Tsujimura, S. Tulipán, M. Turnyanskiy, B. Unterberg, J. Urban, E. Urbonavicius, I. Vakulchyk, S. Valet, B. van Millingen, L. Vela, J.-L. Velasco, M. Vergote, M. Vervier, N. Vianello, H. Viebke, R. Vilbrandt, A. Vorkörper, S. Wadle, F. Wagner, E. Wang, N. Wang, F. Warmer, L. Wegener, J. Weggen, Y. Wei, J. Wendorf, A. Werner, B. Wiegel, F. Wilde, E. Winkler, V. Winters, S. Wolf, J. Wolowski, A. Wright, P. Xanthopoulos, H. Yamada, I. Yamada, R. Yasuhara, M. Yokoyama, J. Zajac, M. Zarnstorff, A. Zeitler, H. Zhang, J. Zhu, M. Zilker, A. Zimbal, A. Zocco, S. Zoletnik, and M. Zuin, "Major results from the first plasma campaign of the wendelstein 7-x stellarator," *Nuclear Fusion*, vol. 57, 10 2017.

[13] C. D. Beidler, H. M. Smith, A. Alonso, T. Andreeva, J. Baldzuhn, M. N. A. Beurskens, M. Borchardt, S. A. Bozhenkov, K. J. Brunner, H. Damm, M. Drevlak, O. P. Ford, G. Fuchert, J. Geiger, P. Helander, U. Hergenhahn, M. Hirsch, U. Höfel, Y. O. Kazakov, R. Kleiber, M. Krychowiak, S. Kwak,

A. Langenberg, H. P. Laqua, U. Neuner, N. A. Pablant, E. Pasch, A. Pavone, T. S. Pedersen, K. Rahbarnia, J. Schilling, E. R. Scott, T. Stange, J. Svensson, H. Thomsen, Y. Turkin, F. Warmer, R. C. Wolf, D. Zhang, I. Abramovic, S. Äkäslompolo, J. Alcusón, P. Aleynikov, K. Aleynikova, A. Ali, A. Alonso, G. Anda, E. Ascasibar, J. P. Bähner, S. G. Baek, M. Balden, M. Banduch, T. Barbui, W. Behr, A. Benndorf, C. Biedermann, W. Biel, B. Blackwell, E. Blanco, M. Blatzheim, S. Ballinger, T. Bluhm, D. Böckenhoff, B. Böswirth, L.-G. Böttger, V. Borsuk, J. Boscary, H.-S. Bosch, R. Brakel, H. Brand, C. Brandt, T. Bräuer, H. Braune, S. Brezinsek, K.-J. Brunner, R. Burhenn, R. Bussiahn, B. Buttenschön, V. Bykov, J. Cai, I. Calvo, B. Cannas, A. Cappa, A. Carls, L. Carraro, B. Carvalho, F. Castejon, A. Charl, N. Chaudhary, D. Chauvin, F. Chernyshev, M. Cianciosa, R. Citarella, G. Claps, J. Coenen, M. Cole, M. J. Cole, F. Cordella, G. Cseh, A. Czarnecka, K. Czerski, M. Czerwinski, G. Czymek, A. da Molin, A. da Silva, A. de la Pena, S. Degenkolbe, C. P. Dhard, M. Dibon, A. Dinklage, T. Dittmar, P. Drewelow, P. Drews, F. Durodie, E. Edlund, F. Effenberg, G. Ehrke, S. Elgeti, M. Endler, D. Ennis, H. Esteban, T. Estrada, J. Fellinger, Y. Feng, E. Flom, H. Fernandes, W. H. Fietz, W. Figacz, J. Fontdecaba, T. Fornal, H. Frerichs, A. Freund, T. Funaba, A. Galkowski, G. Gantenbein, Y. Gao, J. G. Regaña, D. Gates, B. Geiger, V. Giannella, A. Gogoleva, B. Goncalves, A. Goriaev, D. Gradic, M. Grahl, J. Green, H. Greuner, A. Grosman, H. Grote, M. Gruca, O. Grulke, C. Guerard, P. Hacker, X. Han, J. H. Harris, D. Hartmann, D. Hathiramani, B. Hein, B. Heinemann, P. Helander, S. Henneberg, M. Henkel, U. Hergenhahn, J. H. Sanchez, C. Hidalgo, K. P. Hollfeld, A. Hölting, D. Höschen, M. Houry, J. Howard, X. Huang, Z. Huang, M. Hubeny, M. Huber, H. Hunger, K. Ida, T. Ilkei, S. Illy, B. Israeli, S. Jablonski, M. Jakubowski, J. Jelonnek, H. Jenzsch, T. Jesche, M. Jia, P. Junghanns, J. Kacmarczyk, J.-P. Kallmeyer, U. Kamionka, H. Kasahara, W. Kasparek, N. Kenmochi, C. Killer, A. Kirschner, T. Klinger, J. Knauer, M. Knaup, A. Knieps, T. Kobarg, G. Kocsis, F. Köchl, Y. Kolesnichenko, A. Könies, R. König, P. Kornejew, J.-P. Koschinsky, F. Köster, M. Krämer, R. Krampitz, A. Krämer-Flecken, N. Krawczyk, T. Kremeyer, J. Krom, I. Ksiazek, M. Kubkowska, G. Kühner, T. Kurki-Suonio, P. A. Kurz, M. Landreman, P. Lang, R. Lang, S. Langish, H. Laqua, R. Laube, S. Lazerson, C. Lechte, M. Lennartz, W. Leonhardt, C. Li, C. Li, Y. Li, Y. Liang, C. Linsmeier, S. Liu, J.-F. Lobsien, D. Loesser, J. L. Cisquella, J. Lore, A. Lorenz, M. Losert, A. Lücke, A. Lumsdaine, V. Lutsenko, H. Maaßberg, O. Marchuk, J. H. Matthew, S. Marsen, M. Marushchenko, S. Masuzaki, D. Maurer, M. Mayer, K. McCarthy, P. McNeely, A. Meier, D. Mellein, B. Mendelevitch, P. Mertens, D. Mikkelsen, A. Mishchenko, B. Missal, J. Mittelstaedt, T. Mizuuchi, A. Mollen, V. Moncada, T. Mönnich, T. Morisaki, D. Moseev, S. Murakami, G. Náfrádi, M. Nagel, D. Naujoks, H. Neilson, R. Neu, O. Neubauer, T. Ngo, D. Nicolai, S. K. Nielsen, H. Niemann, T. Nishizawa, R. Nocentini, C. Nührenberg, J. Nührenberg, S. Obermayer, G. Offermanns, K. Ogawa, J. Ölmanns, J. Ongena, J. W. Oosterbeek, G. Orozco, M. Otte, L. P. Rodriguez, N. Panadero, N. P. Alvarez, D. Papenfuß, S. Paqay, E. Pawelec, T. S. Pedersen, G. Pelka, V. Perseo, B. Peterson, D. Pilopp, S. Pingel, F. Pisano, B. Plaum, G. Plunk, P. Pölöskei, M. Porkolab, J. Proll, M.-E. Puiatti, A. P. Sitjes, F. Purps, M. Rack, S. Récsei, A. Reiman, F. Reimold, D. Reiter, F. Remp-

pel, S. Renard, R. Riedl, J. Riemann, K. Risse, V. Rohde, H. Röhlinger, M. Romé, D. Rondeshagen, P. Rong, B. Roth, L. Rudischhauser, K. Rummel, T. Rummel, A. Runov, N. Rust, L. Ryc, S. Ryosuke, R. Sakamoto, M. Salewski, A. Samartsev, E. Sánchez, F. Sano, S. Satake, J. Schacht, G. Satheeswaran, F. Schauer, T. Scherer, A. Schlaich, G. Schlisio, F. Schluck, K.-H. Schlüter, J. Schmitt, H. Schmitz, O. Schmitz, S. Schmuck, M. Schneider, W. Schneider, P. Scholz, R. Schrittwieser, M. Schröder, T. Schröder, R. Schroeder, H. Schumacher, B. Schweer, S. Sereda, B. Shanahan, M. Sibilia, P. Sinha, S. Sipliä, C. Slaby, M. Sleczka, W. Spiess, D. A. Spong, A. Spring, R. Stadler, M. Stejner, L. Stephey, U. Stridde, C. Suzuki, V. Szabó, T. Szabolics, T. Szepesi, Z. Szökefalvi-Nagy, N. Tamura, A. Tancetti, J. Terry, J. Thomas, M. Thumm, J. M. Travere, P. Traverso, J. Tretter, H. T. Mora, H. Tsuchiya, T. Tsujimura, S. Tulipán, B. Unterberg, I. Vakulchyk, S. Valet, L. Vanó, P. van Eeten, B. van Milligen, A. J. van Vuuren, L. Vela, J.-L. Velasco, M. Vergote, M. Vervier, N. Vianello, H. Viebke, R. Vilbrandt, A. von Stechow, A. Vorköper, S. Wadle, F. Wagner, E. Wang, N. Wang, Z. Wang, T. Wauters, L. Wegener, J. Weggen, T. Wegner, Y. Wei, G. Weir, J. Wendorf, U. Wenzel, A. Werner, A. White, B. Wiegel, F. Wilde, T. Windisch, M. Winkler, A. Winter, V. Winters, S. Wolf, R. C. Wolf, A. Wright, G. Wurden, P. Xanthopoulos, H. Yamada, I. Yamada, R. Yasuhara, M. Yokoyama, M. Zanini, M. Zarnstorff, A. Zeitler, H. Zhang, J. Zhu, M. Zilker, A. Zocco, S. Zoletnik, and M. Zuin, "Demonstration of reduced neoclassical energy transport in wendelstein 7-x," *Nature*, vol. 596, pp. 221–226, 8 2021.

[14] P. Xanthopoulos, G. G. Plunk, A. Zocco, and P. Helander, "Intrinsic turbulence stabilization in a stellarator," *Physical Review X*, vol. 6, 2016.

[15] J. H. E. Proll, P. Helander, J. W. Connor, and G. G. Plunk, "Resilience of quasi-isodynamic stellarators against trapped-particle instabilities," 9 2015. [Online]. Available: http://arxiv.org/abs/1509.04185http://dx.doi.org/10.1103/PhysRevLett.108.245002

[16] C. D. M. Moreno, J. H. E. Proll, G. G. Plunk, and P. Xanthopoulos, "Exploring zonal flow mediated saturation on stellarators," 9 2020. [Online]. Available: http://arxiv.org/abs/2009.14750

[17] S. I. Krasheninnikov, "On scrape off layer plasma transport," *Physics Letters, Section A: General, Atomic and Solid State Physics*, vol. 283, pp. 368–370, 2001.

[18] S. I. Krasheninnikov, D. A. D'Ippolito, and J. R. Myra, *Recent theoretical progress in understanding coherent structures in edge and SOL turbulence*. Max-Planck-Institut fuer Plasmaphysik, 2008, vol. 74.

[19] D. A. D'Ippolito, J. R. Myra, S. I. Krasheninnikov, G. Q. Yu, and A. Y. Pigarov, "Blob transport in the tokamak scrape-off-layer," *Contributions to Plasma Physics*, vol. 44, pp. 205–216, 4 2004.

[20] U. Stroth, *Plasmaphysik*. Springer, 2018.

[21] F. Jenko, W. Dorland, M. Kotschenreuther, and B. N. Rogers, "Electron temperature gradient driven turbulence," *Physics of Plasmas*, vol. 7, pp. 1904–1910, 5 2000.

[22] J. Citrin, J. Garcia, T. Görler, F. Jenko, P. Mantica, D. Told, C. Bourdelle, D. R. Hatch, G. M. Hogeweij, T. Johnson, M. J. Pueschel, and M. Schneider, "Electromagnetic stabilization of tokamak microturbulence in a high- regime," *Plasma Physics and Controlled Fusion*, vol. 57, 1 2015.

[23] F. I. Parra, "Braginskii fluid equations," 2016.

[24] B. D. Dudson and J. Leddy, "Hermes: Global plasma edge fluid turbulence simulations," *Plasma Physics and Controlled Fusion*, vol. 59, 2017.

[25] A. Stegmeir, D. Coster, A. Ross, O. Maj, K. Lackner, and E. Poli, "Grillix: a 3d turbulence code based on the flux-coordinate independent approach," *Plasma Physics and Controlled Fusion*, vol. 60, p. 035005, 3 2018.

[26] A. N. Simakov and P. J. Catto, "Drift-ordered fluid equations for field-aligned modes in low- collisional plasma with equilibrium pressure pedestals," *Physics of Plasmas*, vol. 10, pp. 4744–4757, 2003.

[27] B. Dudson, H. Muhammed, B. Shanahan, and J. Omotani, "hermes-2 git repo."

[28] D. D. Gray and A. Giorgini, "The validity of the boussinesq approximation for liquids and gases," *International Journal of Heat and Mass Transfer*, vol. 19, pp. 545–551, 5 1976.

[29] K. Bodi, G. Ciraolo, P. Ghendrih, F. Schwander, E. Serre, and P. Tamain, "Impact of the boussinesq approximation in tokamak scrape-off layer turbulence."

[30] S. Braginski, "Transport processes in a plasma," *Reviews of Plasma Physics*, vol. 1, 1 1965. [Online]. Available: https://ui.adsabs.harvard.edu/abs/1965RvPP....1..205B

[31] R. Schneider, X. Bonnin, K. Borrass, D. P. Coster, H. Kastelewicz, D. Reiter, V. A. Rozhansky, and B. J. Braams, "Plasma edge physics with b2-eirene," *Contributions to Plasma Physics*, vol. 46, pp. 3–191, 2 2006.

[32] J. Madsen, V. Naulin, A. H. Nielsen, and J. J. Rasmussen, "Collisional transport across the magnetic field in drift-fluid models," *Physics of Plasmas*, vol. 23, p. 032306, 3 2016.

[33] J. L. Aragón, G. G. Naumis, M. Bai, M. Torres, and P. K. Maini, "Turbulent luminance in impassioned van gogh paintings," *Journal of Mathematical Imaging and Vision*, vol. 30, pp. 275–283, 3 2008.

[34] V. van van Gogh, "Starry night." [Online]. Available: https://artsandculture.google.com/asset/bgEuwDxel93-Pg

[35] M. van Dyke, *An Album of Fluid Motion*. The parabolic press, 1982.

[36] N. Mahdizadeh, "Investigation of three-dimensional turbulent structures in the torsatron tj-k," 2007.

[37] X. Garbet, P. Mantica, C. Angioni, E. Asp, Y. Baranov, C. Bourdelle, R. Budny, F. Crisanti, G. Cordey, L. Garzotti, N. Kirneva, D. Hogeweij, T. Hoang, F. Imbeaux, E. Joffrin, X. Litaudon, A. Manini, D. C. McDonald, H. Nordman, V. Parail, A. Peeters, F. Ryter, C. Sozzi, M. Valovic, T. Tala, A. Thyagaraja, I. Voitsekhovitch, J. Weiland, H. Weisen, A. Zabolotsky, and the JET EFDA Contributors, "Physics of transport in tokamaks," *Plasma Physics and Controlled Fusion*, vol. 46, pp. B557–B574, 12 2004.

[38] P. N. Guzdar, "Ion-temperature-gradient instability in toroidal plasmas," *Physics of Fluids*, vol. 26, p. 673, 1983.

[39] J. Seidl, K. Jirakova, J. Adamek, O. Grover, J. Horacek, M. Hron, and P. Vondracek, "Fluctuations in the scrape-off layer and edge plasma of the compass tokamak," 2018.

[40] B. Nold, "Untersuchung turbulenter strukturen am rand magnetisierter plasmen," 2012.

[41] D. A. D'Ippolito, J. R. Myra, and S. J. Zweben, "Convective transport by intermittent blob-filaments: Comparison of theory and experiment," *Physics of Plasmas*, vol. 18, 2011.

[42] I. Langmuir, "Positive ion currents from the positive column of mercury arcs," *Science*, vol. 58, pp. 290–291, 9 1923.

[43] N. R. Walkden, "Properties of intermittent transport in the mega ampere spherical tokamak," 2014.

[44] M. Kočan, F. P. Gennrich, A. Kendl, and H. W. Müller, "Ion temperature fluctuations in the asdex upgrade scrape-off layer," *Plasma Physics and Controlled Fusion*, vol. 54, 8 2012.

[45] F. Militello, N. R. Walkden, T. Farley, W. A. Gracias, J. Olsen, F. Riva, L. Easy, N. Fedorczak, I. Lupelli, J. Madsen, A. H. Nielsen, P. Ricci, P. Tamain, and J. Young, "Multi-code analysis of scrape-off layer filament dynamics in mast," *Plasma Physics and Controlled Fusion*, vol. 58, p. 105002, 11 2016.

[46] L. Easy, F. Militello, J. Omotani, B. Dudson, E. Havlíčková, P. Tamain, V. Naulin, and A. H. Nielsen, "Three dimensional simulations of plasma filaments in the scrape off layer: A comparison with models of reduced dimensionality," *Physics of Plasmas*, vol. 21, pp. 1–16, 2014.

[47] P. Manz, D. Carralero, G. Birkenmeier, H. W. Müller, S. H. Müller, G. Fuchert, B. D. Scott, and U. Stroth, "Filament velocity scaling laws for warm ions," *Physics of Plasmas*, vol. 20, 10 2013.

[48] B. Shanahan, "Modelling of magnetic null points using bout++," 2016.

[49] P. Helander, "Corrigendum: Theory of plasma confinement in non-axisymmetric magnetic fields (reports on progress in physics (2014) 77 (087001) doi: 10.1088/0034-4885/77/8/087001)," 8 2018.

[50] G. Birkenmeier, "Experimentelle untersuchungen zur struktur und dynamik von driftwellenturbulenz in stellaratorgeometrie," 2012.

[51] B. van Milligen, "Toroidal coordinates," 2009. [Online]. Available: http://fusionwiki.ciemat.es/wiki/Toroidal_coordinates

[52] J. L. V. Lewandowski and M. Persson, "Local magnetic shear in tokamak plasmas," *Plasma Physics and Controlled Fusion*, vol. 37, pp. 1199–1205, 11 1995.

[53] E. W. Weisstein, "The convective operator." [Online]. Available: https://mathworld.wolfram.com/ConvectiveOperator.html

[54] "Field line proxy from ipp webservices," date accessed: 30.03.2022. [Online]. Available: http://esb.ipp-hgw.mpg.de:8280/services/FieldLineProxy?wsdl

[55] J. R. Angus, M. V. Umansky, and S. I. Krasheninnikov, "Effect of drift waves on plasma blob dynamics," *Physical Review Letters*, vol. 108, p. 215002, 5 2012.

[56] J. R. Angus, S. I. Krasheninnikov, and M. V. Umansky, "Effects of parallel electron dynamics on plasma blob transport," *Physics of Plasmas*, vol. 19, 8 2012.

[57] W. Lee, M. V. Umansky, J. R. Angus, and S. I. Krasheninnikov, "Electromagnetic effects on dynamics of high-beta filamentary structures," *Physics of Plasmas*, vol. 22, 1 2015.

[58] D. Carralero, G. Birkenmeier, H. Müller, P. Manz, P. deMarne, S. Müller, F. Reimold, U. Stroth, M. Wischmeier, and E. Wolfrum, "An experimental investigation of the high density transition of the scrape-off layer transport in asdex upgrade," *Nuclear Fusion*, vol. 54, 12 2014.

[59] G. Birkenmeier, P. Manz, D. Carralero, F. Laggner, G. Fuchert, K. Krieger, H. Maier, F. Reimold, K. Schmid, R. Dux, T. Pütterich, M. Willensdorfer, and E. Wolfrum, "Filament transport, warm ions and erosion in asdex upgrade l-modes," *Nuclear Fusion*, vol. 55, p. 033018, 3 2015.

[60] O. Grulke, T. Klinger, M. Endler, and A. Piel, "Analysis of large-scale fluctuation structures in the scrape-off layer of the wendelstein 7-as stellarator," *Physics of Plasmas*, vol. 8, pp. 5171–5180, 12 2001.

[61] M. Endler, L. Giannone, K. McCormick, H. Niedermeyer, A. Rudyj, G. Theimer, N. Tsois, S. Zoletnik, the ASDEX Team, and the W7-AS Team, "Turbulence in the sol of asdex and w7-as," *Physica Scripta*, vol. 51, pp. 610–616, 5 1995.

[62] G. Fuchert, G. Birkenmeier, M. Ramisch, and U. Stroth, "Characterization of the blob generation region and blobby transport in a stellarator," *Plasma Physics and Controlled Fusion*, vol. 58, p. 054005, 5 2016.

[63] J. Bleuel, M. Endler, H. Niedermeyer, M. Schubert, H. Thomsen, and T. W.-A. Team, "The spatial structure of edge fluctuations in the wendelstein 7-as stellarator," *New Journal of Physics*, vol. 4, p. 338, 7 2002.

[64] K. Tanaka, C. Michael, A. Sanin, L. Vyacheslavov, K. Kawahata, S. Murakami, A. Wakasa, S. Okajima, H. Yamada, M. Shoji, J. Miyazawa, S. Morita, T. Tokuzawa, T. Akiyama, M. Goto, K. Ida, M. Yoshinuma, I. Yamada, M. Yokoyama, S. Masuzaki, T. Morisaki, R. Sakamoto, H. Funaba, S. Inagaki, M. Kobayashi, A. Komori, and L. experimental group, "Experimental study of particle transport and density fluctuations in lhd," *Nuclear Fusion*, vol. 46, pp. 110–122, 1 2006.

[65] F. Effenberg, H. Niemann, Y. Feng, J. Geiger, O. Schmitz, Y. Suzuki, A. Ali, T. Barbui, S. Brezinsek, H. Frerichs, M. Jakubowski, R. König, M. Krychowiak, A. P. Sitjes, J. C. Schmitt, and T. S. Pedersen, "Investigation of 3d effects on heat fluxes in performance-optimized island divertor configurations at wendelstein 7-x," *Nuclear Materials and Energy*, vol. 18, pp. 262–267, 2019.

[66] C. Killer, B. Shanahan, O. Grulke, M. Endler, K. Hammond, and L. Rudischhauser, "Plasma filaments in the scrape-off layer of wendelstein 7-x," *Plasma Physics and Controlled Fusion*, vol. 62, 8 2020.

[67] B. Shanahan and P. Huslage, "Filament simulations in regions of highly-varying parallel connection length," *Journal of Plasma Physics*, 2020.

[68] B. Shanahan, B. Dudson, and P. Hill, "The effects of non-uniform drive on plasma filaments," *Journal of Physics: Conference Series*, vol. 1125, 2018.

[69] B. Dudson, M. Umansky, X. Xu, P. Snyder, and H. Wilson, "Bout++: A framework for parallel plasma fluid simulations," *Computer Physics Communications*, vol. 180, pp. 1467–1480, 9 2009.

[70] B. D. Dudson, J. Madsen, J. Omotani, P. Hill, L. Easy, and M. Løiten, "Verification of bout++ by the method of manufactured solutions," *Physics of Plasmas*, vol. 23, 2016.

[71] T. Ahmadi, H. Tanabe, and Y. Ono, "Two-dimensional resistive mhd simulation of the optimized plasma formation in the spherical tokamaks," *Nuclear Fusion*, vol. 61, p. 066001, 6 2021.

[72] S. Raj, N. Bisai, V. Shankar, and A. Sen, "Effects of nitrogen seeding in a tokamak plasma," *Physics of Plasmas*, vol. 27, p. 122302, 12 2020.

[73] G. Decristoforo, A. Theodorsen, J. Omotani, T. Nicholas, and O. E. Garcia, "Numerical turbulence simulations of intermittent fluctuations in the scrape-off layer of magnetized plasmas," *Physics of Plasmas*, vol. 28, p. 072301, 7 2021.

[74] A. Hasegawa, C. G. Maclennan, and Y. Kodama, "Nonlinear behavior and turbulence spectra of drift waves and rossby waves," *Physics of Fluids*, vol. 22, p. 2122, 1979.

[75] A. Hasegawa and M. Wakatani, "Plasma edge turbulence," *Physical Review Letters*, vol. 50, pp. 682–686, 2 1983.

[76] S. Balay, "Petsc - portable, extensible toolkit for scientific computation," 2019. [Online]. Available: https://www.mcs.anl.gov/petsc/index.html

[77] S. Balay, S. Abhyankar, M. F. Adams, S. Benson, J. Brown, P. Brune, K. Buschelman, E. M. Constantinescu, L. Dalcin, A. Dener, V. Eijkhout, W. D. Gropp, V. Hapla, T. Isaac, P. Jolivet, D. Karpeev, D. Kaushik, M. G. Knepley, F. Kong, S. Kruger, D. A. May, L. C. McInnes, R. T. Mills, L. Mitchell, T. Munson, J. E. Roman, K. Rupp, P. Sanan, J. Sarich, B. F. Smith, S. Zampini, H. Zhang, H. Zhang, and J. Zhang, "Petsc web page," 2021. [Online]. Available: https://petsc.org/

[78] S. Balay, W. D. Gropp, L. C. McInnes, and B. F. Smith, "Efficient management of parallelism in object oriented numerical software libraries," E. Arge, A. M. Bruaset, and H. P. Langtangen, Eds. Birkhäuser Press, 1997, pp. 163–202.

[79] J. Terry, S. G. Baek, and S. Ballinger, "Design of a gas-puff imaging diagnostic for w7-x," *60th Annual Meeting of the APS Division of Plasma Physics*, vol. Volume 63, p. 11, 2018. [Online]. Available: http://meetings.aps.org/link/BAPS.2018.DPP.BP11.59

[80] B. Shanahan, B. Dudson, and P. Hill, "Fluid simulations of plasma filaments in stellarator geometries with bsting," *Plasma Physics and Controlled Fusion*, vol. 61, 2019.